J. Fluid Mech. (2007), *vol.* 592, *pp.* 413–446.
doi:10.1017/S0022112007008671 Printed in the United Kingdom

The physics of vortex merger and the effects of ambient stable stratification

LAURA K. BRANDT AND KEIKO K. NOMURA

Department of Mechanical and Aerospace Engineering, University of California, San Diego, La Jolla, California, 92093-0411, USA

(Received 15 November 2006 and in revised form 7 August 2007)

The merging of a pair of symmetric, horizontally oriented vortices in unstratified and stably stratified viscous fluid is investigated. Two-dimensional numerical simulations are performed for a range of flow conditions. The merging process is resolved into four phases of development and key underlying physics are identified. In particular, the deformation of the vortices, explained in terms of the interaction of vorticity gradient, $\nabla\omega$, and rate of strain, $\boldsymbol{S}$, leads to a tilt in ω contours in the vicinity of the center of rotation (a hyperbolic point). In the diffusive/deformation phase, diffusion of the vortices establishes the interaction between $\nabla\omega$ and mutually induced $\boldsymbol{S}$. During the convective/deformation phase, induced flow by filaments and, in stratified flow, baroclinically generated vorticity (BV), advects the vortices thereby modifying $\boldsymbol{S}$, which, in general, may enhance or hinder the development of the tilt. The tilting and diffusion of ω near the center hyperbolic point causes ω from the core region to enter the exchange band where it is entrained. In the convective/entrainment phase, the vortex cores are thereby eroded and ultimately entrained into the exchange band, whose induced flow becomes dominant and transforms the flow into a single vortex. The critical aspect ratio, associated with the start of the convective/entrainment phase, is found to be the same for both the unstratified and stratified flows. In the final diffusive/axisymmetrization phase, the flow evolves towards axisymmetry by diffusion. In general, the effects of stratification depend on the ratio of the diffusive time scale (growth of cores) to the turnover time (establishment of BV), i.e. the Reynolds number. A crossover Reynolds number is found, above which convective merging is accelerated with respect to unstratified flow and below which it is delayed.

1. Introduction

The merging of two co-rotating vortices has drawn much attention due to its fundamental and practical significance in engineering and environmental flows. It is an elementary vortex interaction which plays a significant role in the transfer of energy and enstrophy across scales in transitional flows and two- and three-dimensional turbulence. It may also occur in the near-field wake of an aircraft, just downstream from the wing tip and outboard edge flap, thereby forming the primary wake vortices (Brandt & Iversen 1977; Rossow 1977). Such vortices have long lifetimes and can be hazardous to following aircraft. Atmospheric conditions such as stable density stratification can influence the dynamics of the vortices.

In an unstratified fluid, a pair of (symmetric) vortices of equal circulation, Γ, and equal core size, a, separated by a distance, b, will rotate about each other due to the mutually induced velocity. If the aspect ratio a/b exceeds some critical

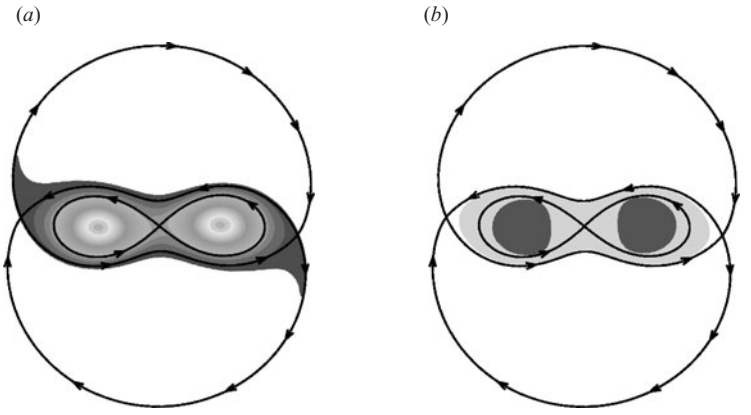

FIGURE 1. Streamlines in co-rotating frame with (a) vorticity contours superimposed and (b) shading indicating flow region analysis based on velocity gradient tensor (dark grey, cores; light grey, exchange band; white, outer-recirculation region, i.e. filaments), for $Re_\Gamma = 5000$, $Fr = \infty$ at $t_c^* = 1.88$.

value, $(a/b)_{cr}$, vortex merger results. Much of the previous work on symmetric vortex merger has focused on the determination of $(a/b)_{cr}$ (Rossow 1977; Saffman & Szeto 1980; Overman & Zabusky 1982; Griffiths & Hopfinger 1987; Meunier *et al.* 2002). Using contour dynamics of uniform vortices, Saffman & Szeto (1980) and Overman & Zabusky (1982) find a critical separation distance, above which equilibrium configurations of non-circular vortices can exist, and below which the vortices are unstable and merge. A linear stability analysis of such equilibrium configurations is performed by Dritschel (1985) which associates the instability with boundary deformation. In general, experimental measurements (viscous, non-uniform vortices) of $(a/b)_{cr}$ have varied due to difficulties of measurement and inconsistent definitions of a_{cr} and b_{cr}. Meunier *et al.* (2002) present a method for determining a_{cr} from experimental data by considering the critical condition as the transition from a purely viscous regime to a convective regime.

The physical mechanism associated with merger was considered by Melander, Zabusky & McWilliams (1988). They examine the flow in a co-rotating reference frame which reveals the differential motion and associated flow structure. This is illustrated in figure 1(a), which shows the principal streamlines (separatrices) defining three distinct regions in the flow. The *inner core regions* consist of closed streamlines encircling each individual vorticity maximum and correspond to the primary vortices. The *exchange band* consists of closed streamlines encompassing both inner core regions, and corresponds to fluid circulating (exchanged) between the two vortices. The two *outer recirculation regions* consist of fluid which circulates in the opposite sense (in the co-rotating frame) to that of the cores and exchange band. Melander *et al.* (1988) explain the occurrence of merger in terms of the vorticity distribution relative to the separatrices. In particular, when vorticity enters the outer-recirculation regions, differential rotation causes the formation of filaments, which breaks the elliptical symmetry of the flow. This modifies the orientation of the vorticity contours with respect to the streamlines and leads to merger through an inviscid axisymmetrization process. The process of axisymmetrization was studied in detail for an isolated elliptical vortex by Melander, McWilliams & Zabusky (1987). They indicate that both filaments and gradient intensification in the core contribute to asymmetric vorticity; the filaments, however, being the dominant contributor. A subsequent study by

Dritschel (1998) shows that non-axisymmetry may persist indefinitely in an inviscid flow, suggesting that it is the presence of diffusion which promotes axisymmetrization. Although the importance of the exchange band was noted, Melander *et al.* (1988) indicate that merger is driven by filament formation.

More recently, Cerretelli & Williamson (2003) have considered these ideas further, and demonstrate that merger is due to the antisymmetric part of the vorticity field, which is also considered to be primarily associated with the filaments. They suggest that vorticity enters the outer-recirculation region through viscous or turbulent diffusion, thereby initiating filament formation. Meunier (2001) explains the role of the filaments and accompanying reduction in b in terms of conservation of angular momentum. A simple model is developed and although the initial reduction in b is well predicted, it does not predict the dominant motion of the vortices, suggesting that some other mechanism is present (Meunier, Le Dizes & Leweke 2005). Velasco Fuentes (2005) finds that filamentation does not always lead to merger and, in the case of steep vorticity profiles, merger begins before filamentation takes place. The stability analysis by Dritschel (1985) also precludes the requirement of filamentation for convective merger. Huang (2005) analyses the flow in terms of Lagrangian flow structures and shows that the 'sheetlike structure' emanating from the opposite vortex, which includes both filament and exchange band fluid, is responsible for the induced merging velocity. The formation of these structures is attributed to a tilt of the major axes of the vortices and the connecting line between the vortex centroids. How the tilt is established was not explained. Brandt & Nomura (2006) determine the relative contribution of each of the flow regions and show that the exchange band vorticity is the dominant contributor to the reduction in b. The associated physics are described in terms of the interaction of vorticity gradient, $\nabla\omega$, and rate of strain, $\boldsymbol{S}$, near the center of rotation, through which the tilt in the vorticity contours is established. This leads to the entrainment of core fluid into the exchange band, which ultimately transforms into a single vortex. Details of the analysis, which yield a generalized description of merger, are presented in this study.

The effects of stable density stratification on vortex pair dynamics have been considered in a number of studies. The merging of *vertically* oriented co-rotating vortices have been considered in the context of geophysical flows. Two-layer fluid systems (Griffiths & Hopfinger 1987) and three-dimensional flows (Dritschel 2002; von Hardenberg *et al.* 2000) have been studied. Results show that increasing the vertical aspect ratio, a/H (where H is the half-height used to indicate the level of stratification) reduces the critical distance for merger. Regarding *horizontally* oriented vortices, studies of stably stratified shear layers suggest that stratification acts to suppress pairing and merging of Kelvin–Helmholtz billows. A numerical study by Patnaik, Sherman & Corcos (1976) indicates that strong stratification hinders the growth of billows. Laboratory experiments by Koop & Browand (1979) show that the average number of vortex pairings that occur for a fixed Reynolds number decreases for increasing levels of stratification. Schowalter, Van Atta & Lasheras (1994) conclude that stratification both enhances and weakens the vortex cores; baroclinically generated opposite-signed vorticity weakens vortex cores, while baroclinically generated same-signed vorticity strengthens them. Pawlak & Armi (1998, 2000) report that the shear layer is significantly altered by the presence of stratification and may in some cases cause the vortex cores to be shed from Kelvin–Helmholtz billows. Although the effects of stable stratification have been considered for the case of horizontally oriented *counter-rotating* vortex pairs (see Nomura *et al.* 2006 for a review), no previous studies have considered the case of a horizontally oriented co-rotating vortex pair in a stably stratified fluid.

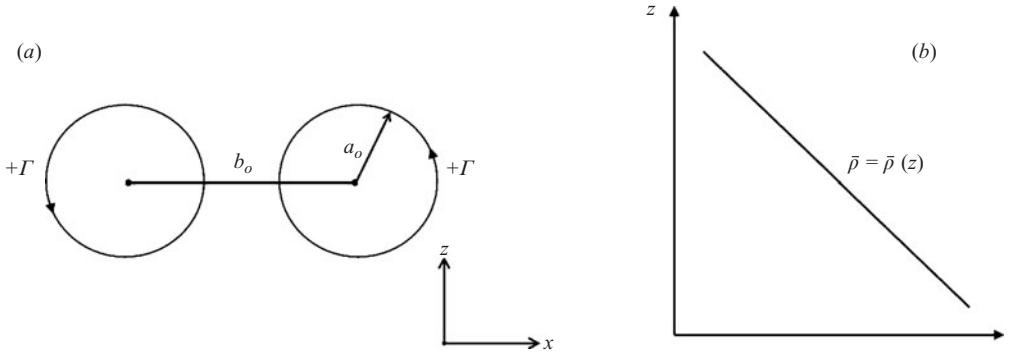

FIGURE 2. Coordinate system and initial conditions for co-rotating vortex pair and uniform stable stratification: (*a*) initial symmetric vortices with equal circulation strength, Γ_o, and centres separated by a distance, b_o; (*b*) background linear density profile $\bar{\rho}(z)$.

The objective of the present study is to investigate the merging process of a pair of horizontal co-rotating vortices, with and without stable stratification in the ambient fluid. Two-dimensional numerical simulations are performed for a range of flow conditions. We note that the stratified flows considered here are associated with relatively weak stratification, which effectively introduces a disturbance to the merging process. By determining its effects, we obtain further insight and understanding of the fundamental physics of vortex interaction and merging. Results of the study provide details of the induced flow and $\boldsymbol{S}$ fields. The deformation of the vortices is described in terms of the interaction of $\nabla\omega$ and $\boldsymbol{S}$. The effects of Reynolds number and Froude number (stratification level) are considered. A new generalized description of the merging process is developed which allows for a more explicit determination of the critical aspect ratio and assists in accounting for the effects of stratification. The critical aspect ratio is evaluated and found to be the same in both the unstratified and stratified flows.

The numerical simulations and flow parameters are described in § 2. Results are presented in § 3. The general development of the unstratified and stratified flows is first examined (§ 3.1), and the physical mechanisms of vortex merger in unstratified flow are then analyzed (§ 3.2). This provides a framework with which to study the effects of stratification on the merger process. Analysis of the stratified flow is carried out (§ 3.3 and § 3.4); a generalized description of the merging process is then developed and the effects of Reynolds number are considered (§ 3.5). A summary is given in § 4.

2. Numerical simulations

Two-dimensional numerical simulations of a co-rotating vortex pair in an initially uniform stably stratified fluid are performed for this study. Figure 2 shows the initial flow geometry and coordinate system. Here, the spatial coordinates, x, z, correspond to the transverse and vertical directions, respectively. The governing equations with the Boussinesq approximation are:

$$\nabla \cdot \boldsymbol{v} = 0 \tag{2.1}$$

$$\frac{\partial \boldsymbol{v}}{\partial t} + \boldsymbol{v} \cdot \nabla \boldsymbol{v} = -\frac{1}{\rho_o}\nabla p + \nu \nabla^2 \boldsymbol{v} + \rho' \boldsymbol{g} \tag{2.2}$$

$$\frac{\partial \rho}{\partial t} + \boldsymbol{v} \cdot \nabla \rho = \kappa \nabla^2 \rho \tag{2.3}$$

where ρ_o is a constant reference density, ν is the kinematic viscosity, $\boldsymbol{g} = (0, -g)$ is the gravitational acceleration, and κ is the thermal diffusivity. In the above equations, $\boldsymbol{v} = (u, w)$ is the instantaneous velocity, p is the deviation of the pressure from its hydrostatic value and ρ' is the deviation of the density from the background density, i.e. the instantaneous density is $\rho = \rho_o + \overline{\rho}(z) + \rho'(x, z, t)$, where $\overline{\rho}(z)$ corresponds to the imposed uniform stable stratification, $\mathrm{d}\overline{\rho}/\mathrm{d}z$ (figure 2*b*).

The initial base flow consists of the superposition of two Lamb-Oseen (Gaussian) co-rotating (anti-clockwise) vortices, which is representative of the initial vortices in Meunier & Leweke (2001). The corresponding vorticity distribution is given by

$$\omega(x, z, t_o) = \Omega_o \exp\left(\frac{-((x - x_1)^2 + (z - z_1)^2)}{a_o^2}\right) + \Omega_o \exp\left(\frac{-((x - x_2)^2 + (z - z_2)^2)}{a_o^2}\right), \tag{2.4}$$

where $\Omega_o = \Gamma_o/\pi a_o^2$ is the peak vorticity, a_o is the initial vortex radius and (x_1, z_1) and (x_2, z_2) are the initial coordinates of the two vortex centroids. The geometry of the vortex pair is specified by the dipole aspect ratio, a_o/b_o, where $b_o = |x_2 - x_1|$ is the initial vortex separation distance (figure 2*a*). Here, a_o is based on the vorticity second moment, $\int r^2 \omega \, \mathrm{d}A / \int \omega \, \mathrm{d}A$, where r is the radial distance from a vortex centroid, ω is vorticity, and the integral is performed over a single vortex. In the simulations presented, we consider a fixed initial aspect ratio of $a_o/b_o = 0.157$.

The relevant nondimensional parameters are now defined. The characteristic length scales of the flow are b_o and a_o. The velocity scale is the initial (rotational) velocity of the vortices, $W_o = \Gamma_o/2\pi b_o$, where Γ_o is the initial vortex circulation. The stratification is characterized by the buoyancy frequency, N, where $N^2 = -(g/\rho_o)\mathrm{d}\overline{\rho}/\mathrm{d}z$. A convective time scale of the flow is the rotational period, $t_c = 2\pi^2 {b_o}^2/\Gamma_o$. A viscous time scale is defined as $t_v = a_o^2/4\nu$. The buoyancy time scale is $t_s = \pi/N$, which is the buoyancy period. The circulation Reynolds number used here is given by

$$Re_\Gamma = \frac{2\pi W_o b_o}{\nu} = \frac{\Gamma_o}{\nu} = \frac{8\pi^2}{(a_o/b_o)^2}\frac{t_v}{t_c}. \tag{2.5}$$

The Froude number is defined as

$$Fr = \frac{\Gamma_o}{2\pi b_o^2 N} = \frac{t_s}{t_c}. \tag{2.6}$$

The Prandtl number is $Pr = \nu/\kappa$.

The range of Reynolds number considered, $2000 \leqslant Re_\Gamma \leqslant 5000$, is comparable to laboratory experiments (Meunier & Leweke 2001). The Froude numbers considered are $Fr = 2$, 3 and 5, which cover a range of conditions corresponding to relatively strong ($Fr = 2$) moderate ($Fr = 3$) and weak ($Fr = 5$) stratification. In general, however, stratification is not a dominating effect in the flows considered ($Fr > 1$), and vortex merger will result. In flows with lower Fr, stratification will hinder fluid motion and/or result in significant internal waves. Such flows are beyond the scope of this study. The case of $Fr = \infty$ corresponding to an unstratified flow is also considered. The Prandtl number in the simulations is $Pr = 1.0$.

The numerical solution procedure is based on a second order finite difference scheme with second order Adams-Bashforth time integration (Gerz, Schumann & Elghobashi 1989). In these two-dimensional calculations, the computational domain has dimensions of $L_x = L_z = 24b_o$, and employs 2048^2 grid points. This allows approximately 27 grid points across the core of each vortex (i.e. $2a_o$). Resolution tests using 54 grid points across the core showed minimal differences in computed

quantities (e.g. the integrated quantity, a, differed by a maximum of 0.4 %) thereby indicating a resolution-independent solution. Domain size independence was also examined. In these simulations, the periodic boundary conditions used are, in general, inconsistent with the nonzero circulation of this flow. Rather than attempting to negate the circulation by introducing an unphysical background flow, such as done in Melander *et al.* (1987), we consider a sufficiently large domain to minimize the effect of neighboring vortices and far-field flow interaction. Domain size tests compared both integrated (e.g. a) and local (e.g. strain rate, vorticity) quantities for a range of $L_x = L_z = L$ domain sizes and showed maximum differences of 0.01 % between $L = 12b_o$ and $L = 24b_o$ results. In addition, the induced flow from neighboring vortices was computed and found to be negligible.

3. Results

In the majority of the results presented, time is nondimensionalized by t_c (reference rotation period).

3.1. *General flow development*

Figures 3 and 4 show time sequences of vorticity contours illustrating the basic development of unstratified ($Fr = \infty$) and stratified ($Fr = 3$) flows, respectively, at $Re_\Gamma = 5000$. In both flows, due to the mutually induced velocity, the two vortices rotate about each other in the anti-clockwise direction. Before merging is initiated, the rate of rotation is nearly equal to that of a two-point vortex system, $\Gamma/\pi b^2$. The unstratified flow (figure 3) develops as observed in previous studies. At early times (figure 3*a–e*, $t_c^* \leqslant 1.31$), the vortices grow due to viscous diffusion. They also adjust to the induced strain field, which results in an elliptic deformation of the cores. Later in time (figure 3*f–h*, $t_c^* \geqslant 1.45$), more significant deformation is observed, particularly at the lowest vorticity contour levels. At the outer locations of the vortex pair, filamentation occurs, and in the vicinity of the center of rotation, a tilt in the vorticity contours develops. The major axes of the vortices are tilted with respect to the connecting line of the vortices; subsequently, the vortex centers are rapidly drawn towards and around each other (figure 3*i–k*, $t_c^* \geqslant 1.97$). The rate of rotation of the vortex pair increases due to conservation of angular momentum. The inward spiral motion leaves the filaments wrapped around the vortex centers (figure 3*l*). At late times (not shown), the overall flow consists of essentially a single structure within which the two vorticity maxima revolve. In time, the two maxima eventually disappear by viscous diffusion. A single vortex is established.

In the stratified flow (figure 4), as the vortex pair rotates, it stirs the stably stratified ambient fluid. After approximately half a revolution, opposite-signed vorticity appears at the periphery of the outer-recirculation regions (figure 4*c*, $t_c^* = 0.78$). This is due to baroclinic torque generation, as will be discussed in § 3.3. There is a slight decrease in the rate of rotation of the vortex pair. Later in time (figure 4*d*, $t_c^* = 1.07$), both opposite-signed vorticity and same-signed vorticity occur just outside and within the outer-recirculation regions. Filamentation and tilting of the primary vortices and the motion of the vortices towards each other all occur earlier in time (figure 4*e*, $t_c^* = 1.31$). At late times (figure 4*g–i*, $t_c^* \geqslant 1.69$), the structure of the vorticity field is more complex and consists of alternating-signed vorticity patches and filaments. Some reduction in the vertical scale of the flow is also observed.

In previous studies (Melander *et al.* 1988; Meunier 2001; Cerretelli & Williamson 2003), vortex merging in a viscous unstratified fluid is considered to occur in three

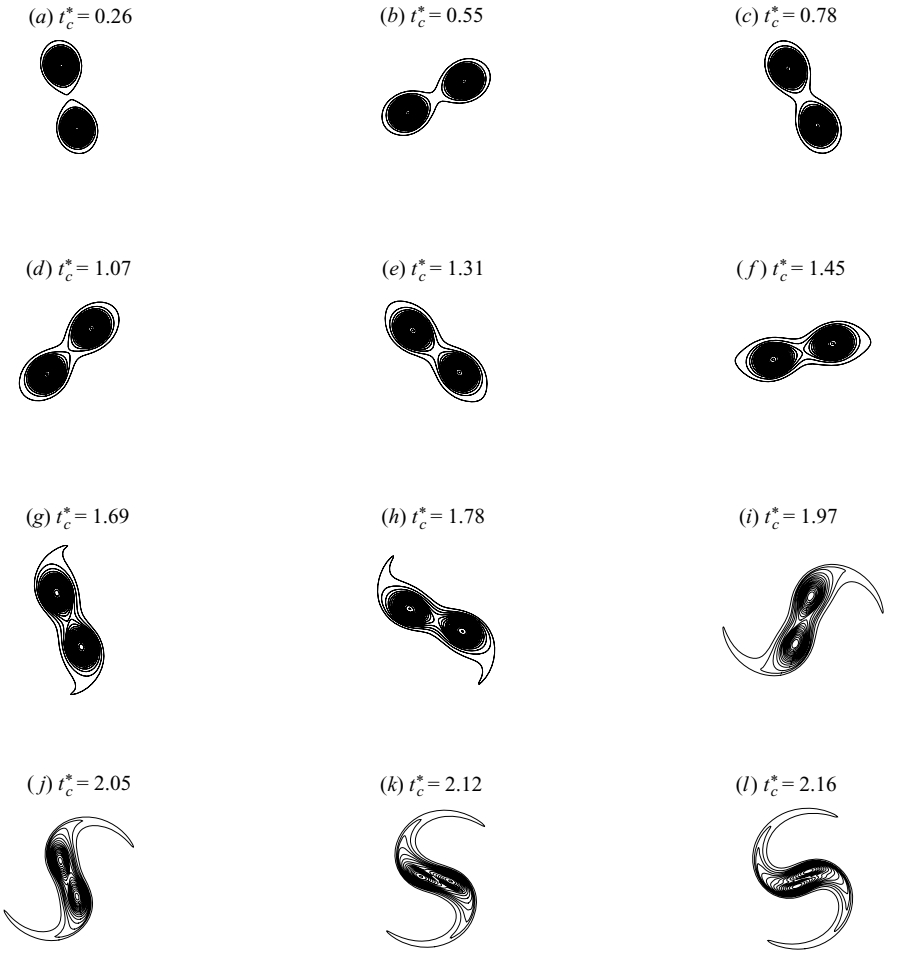

FIGURE 3. Line plots of vorticity contours for $Re_\Gamma = 5000$, $Fr = \infty$.

phases: the first diffusive phase, the convective phase, and the second diffusive phase; the phases designated by the behaviour of the separation distance, $b(t)$, and the core size, $a(t)$. Time development of $b^* = b/b_o$ and $a^{*2} = a^2/{b_o}^2$ are given in figure 5. Note that the core size in figure 5(b), a_ω, is defined in terms of the second moment of vorticity, and that in figure 5(c), a_θ, in terms of the radial location of maximum azimuthal velocity (averaged over azimuthal coordinate). At $t_c^* = 0$, $a_\theta = 1.12\, a_\omega$, as expected for a Lamb-Oseen vortex. We note that a_θ will assist in the analysis of stratified flow.

During the first diffusive phase in the unstratified flow, $b(t)$ remains relatively constant (figure 5a) while $a(t)$ grows by viscous diffusion (figure 5b, c). The development of both $a_\omega^2(t)$ and $a_\theta^2(t)$ is linear and essentially follows the behavior of a single vortex,

$$a^2 = c^2 \nu t + {a_o}^2 \tag{3.1}$$

or, in non-dimensional form,

$$a^{*2} = c^2 \frac{2\pi^2}{Re_\Gamma} t_c^* + {a_o}^{*2}. \tag{3.2}$$

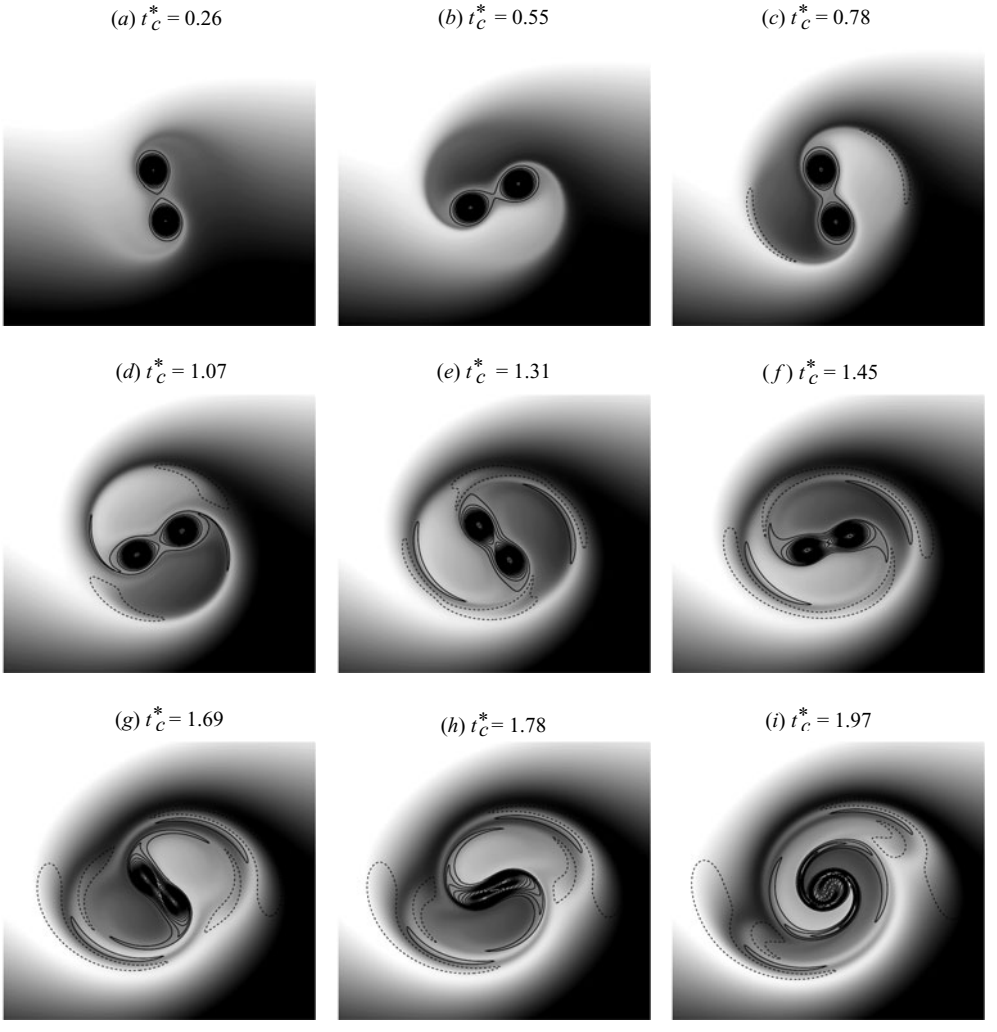

FIGURE 4. Vorticity contours (solid line, $\omega > 0$; dashed line, $\omega < 0$) superimposed on density field (shading) for $Re_\Gamma = 5000$, $Fr = 3$.

The growth rate constants for $a_\omega^2(t)$ and $a_\theta^2(t)$ are determined to be $c_\omega = 2.11$ and $c_\theta = 2.17$, respectively. We note that for a Lamb-Oseen vortex, $c_\omega = 2.0$ and $c_\theta = 2.24$ (Saffman 1992). The end of the diffusive phase is typically marked by the deviation of $a^2(t)$ from its linear growth (transition from a diffusive- to convective-dominated process). This occurs for both $a_\omega^2(t)$ and $a_\theta^2(t)$ at $t_c^* \sim 1.7$ (figure 5*b*, *c*, $Fr = \infty$), which corresponds to a critical core size of $(a_\omega/b_o)_{cr} \sim 0.23$, comparable to values reported by Meunier *et al.* (2002). The critical aspect ratio will be further considered in § 3.5. The convective phase corresponds to the predominant reduction in $b^*(t)$. Note that in the latter part of this phase, $b^*(t)$ exhibits a rapid and nearly linear decrease. The convective phase terminates when b reaches approximately $0.20b_o - 0.25b_o$, at which point the inward velocities at the centroids are nearly zero. The second diffusive phase is characterized by a slow reduction in $b^*(t)$ (not shown) as the two ω maxima diffuse into one. Beyond this time, development of $a^2(t)$ (for single merged vortex) eventually returns to linear growth by diffusion (Cerretelli & Williamson 2003).

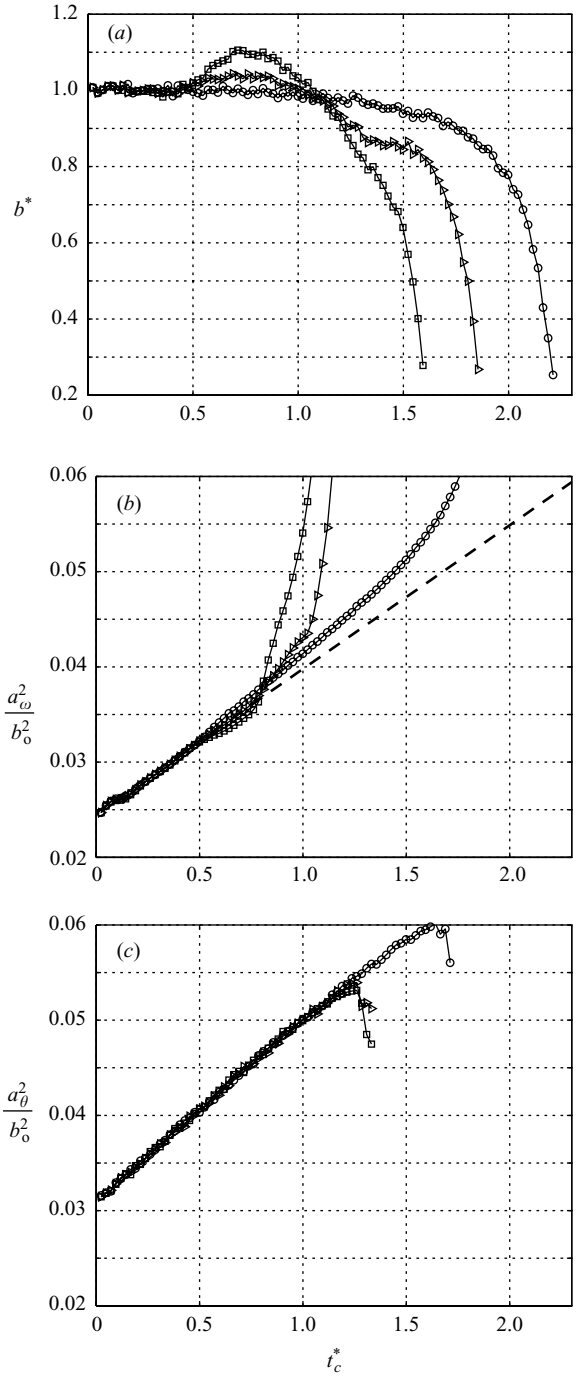

FIGURE 5. Time development of (*a*) separation distance, $b^*(t) = b(t)/b_o$, (*b*) core size evaluated by second moment, $a_\omega^2(t)/b_o^2$, (*c*) core size evaluated by maximum azimuthal velocity, $a_\theta^2(t)/b_o^2$. The dashed line in (*b*), which corresponds to (3.3) where $c' = c_\theta/1.12 = 1.94$. Symbols: ○, $Fr = \infty$; ▷, $Fr = 3$; □, $Fr = 2$.

In the stratified flows (figure 5*a*; $Fr = 2, 3$), a slight increase in b^* is initiated at approximately $t^* = 0.5$ (see § 3.4), followed by an earlier decrease as compared with the $Fr = \infty$ flow. The rate of increase and initial decrease in $b^*(t)$ is greater with increased stratification ($Fr = 2$). In both stratified flows, the rapid linear decrease in $b^*(t)$ exhibits nearly the same slope as that of the unstratified flow. Overall, convective effects and merger, as indicated by $b^*(t)$, occur earlier in the stratified flows. From figure 5(*b*), we see that the initial development of $a_\omega^2(t)$ is linear. However, since a_ω^2 is evaluated by integration of ω, which includes generated vorticity (figure 4), it does not solely describe the growth by viscous diffusion during this time. In contrast, the quantity $a_\theta^2(t)$ in figure 5(*c*) does not have this ambiguity and is used here to indicate the core growth in stratified flow. From figure 5(*c*), we observe that $a_\theta^2(t)$ grows linearly and with the same growth rate as that in unstratified flow, as expected since they have the same Re_Γ. Note that the dashed line in figure 5(*b*) corresponds to

$$a^2 \;=\; \left(\frac{c_\theta}{1.12}\right)^2 \nu t + {a_o}^2 \;=\; {c'}^2 \nu t + {a_o}^2, \tag{3.3}$$

where $c' = 1.94$ based on the above results and $(a_o/b_o) = 0.157$ (a_o based on a_ω). This allows us to evaluate an *effective* a^2 for stratified flows that is consistent with the defined a_o (to be used in § 3.5). As also observed in figure 5(*c*), $a_\theta^2(t)$ indicates deviation from linear behavior earlier in the stratified flows, and it occurs at approximately the same time, $t_c^* \sim 1.25$, for both $Fr = 3$ and $Fr = 2$. From the results in figure 5, we find that $b^*(t)$ and $a^*(t)$ show convective effects initiating at different times. Thus, the evaluation of a critical aspect ratio and the demarcation of the first diffusive phase and convective phase are unclear. These issues will be considered in the following sections and resolved in § 3.5. As in the unstratified flow, the convective phase terminates when b reaches approximately $0.2b_o$, and the second diffusive phase allows for the final reduction in $b^*(t)$ (see figure 17).

3.2. *Vortex merging: unstratified flow*

The basic physical mechanisms of the merging process are now considered. Following Brandt & Nomura (2006), we examine the induced flow of each of the distinct flow regions in the co-rotating frame of reference. The regions are identified in the simulation results as follows. The inner-recirculation region (cores and exchange band) and outer-recirculation (filaments) region are distinguished by the *sign* of ω in the co-rotating frame. The cores and exchange band are distinguished by considering the second invariant of the velocity gradient tensor (co-rotating frame), $II = (\boldsymbol{\omega}^2/2 - \boldsymbol{S}^2)/2$ (Nomura & Post 1998). Thus, $II > 0$ corresponds to rotation-dominated regions, which effectively characterizes the cores, and $II < 0$ corresponds to strain-dominated regions, which characterizes the exchange band. We note that in two-dimensional flow, $II > 0$ is equivalent to the λ_2 criterion for vortex identification of Jeong & Hussain (1995). Figure 1(*b*) illustrates the three defined regions used in the analysis sampling. Although the identification scheme is unable to isolate the exchange band strictly, it is the strain-dominated regions that have particular dynamic significance and the sample effectively reveals key aspects of the flow development. The sampling method is effective through most of the convective phase of the flow. Beyond this, a fundamental transformation of the flow structure occurs and the identification procedure is terminated, since the rotation rate can no longer be accurately evaluated. With the flow regions identified, the velocity field induced by each region is computed using the Biot–Savart law.

Figure 6 shows the contribution of the flow regions to the *change* in $b^*(t)$, $\Delta b^*_{region}(t)$. This is determined by evaluating the inward velocity induced at the vortex centroids by each region and integrating it in time. The contribution of the filaments (figure 6*b*, $Fr = \infty$), which begins at $t^*_c \sim 1$, corresponds to the initial, slow decrease in $b^*(t)$. The contribution of the exchange band (figure 6*c*), which begins at $t^*_c \sim 1.7$, is associated with the predominant and rapid decrease in $b^*(t)$ during the latter part of the convective phase. We note that the contribution of the inner cores (not shown) oscillates about zero through the diffusive phase (Brandt & Nomura 2006). In the flow considered here, just after $t^*_c \sim 1.7$, the cores contribute to an increase in $b^*(t)$.

Figure 7 shows the induced flow fields of each of the regions in the vicinity of the center of rotation (a hyperbolic point) at two times ($t^*_c = 1.69$, 1.97). At $t^*_c = 1.69$ (figure 7*a–c*), the velocities induced by the cores are still dominant; those of the filaments are at least an order of magnitude less due to the relatively low ω in this region. However, an inward component of the velocities between the cores is detected in the filament-induced flow field (figure 7*b*), consistent with the results in figure 6(*b*). From figure 7(*a*), we observe a tilt in the lowest-level ω contours and the associated misalignment of ω with the streamlines (the actual streamlines are close to those of the core-induced velocities at this time). The exchange-band-induced velocity field (figure 7*c*) corresponds to weak circulatory motion between the two cores. At $t^*_c = 1.97$ (figure 7*d–f*), the ω contours show vorticity from the core regions entrained into the exchange band. The velocities induced by the exchange band (figure 7*f*) thereby become significant with magnitudes comparable to those induced by the cores and correspond to predominantly rotational motion about the center of the vortex pair. In time, as more of the core vorticity is entrained into the exchange band, this induced flow strengthens and eventually dominates the flow.

The overall merging process is now considered. As discussed earlier, the model of Meunier *et al.* (2005) considers the effect of the filaments, and although it predicts quite well the initial gradual reduction of $b^*(t)$, it fails to predict the final rapid reduction. However, as shown in figure 6, the dominant reduction in $b^*(t)$ is due to the exchange band. This is the missing mechanism in the model. The process is initiated when core vorticity enters the exchange band through a tilt in ω contours near the center hyperbolic point (figure 7*a*). Vorticity is advected away from its source core and into the exchange band; the inner cores are thereby stripped and eroded (figure 7*d*). At some point, the cores themselves are entrained. This corresponds to the rapid linear decrease in $b^*(t)$ associated with the induced flow by the exchange band (figure 6*c*). We therefore consider the *convective phase* to consist of two components: (i) induced motion of filaments advecting the two vortices towards each other, and (ii) core erosion and entrainment by the exchange band, the latter transforming the structure of the flow to essentially a single vortex.

In order to understand the deformation of the vortices, and, in particular, how the tilt in ω contours develops, we first consider the structure and behavior of the rate of strain, $\boldsymbol{S}$. Since this is a two-dimensional incompressible flow, the two principal eigenvalues of $\boldsymbol{S}$ are equal in magnitude and opposite in sign, and the corresponding eigenvectors are easily computed. As indicated in Brandt & Nomura (2006), early in the first diffusive phase, the strain rate field is characteristic of two separate vortices, i.e. a band of high strain surrounds each of the cores, and the associated eigenvectors are oriented 45° from the radial direction. During this phase, as viscous diffusion increases the core size, the strain bands correspondingly spread outward. The strain

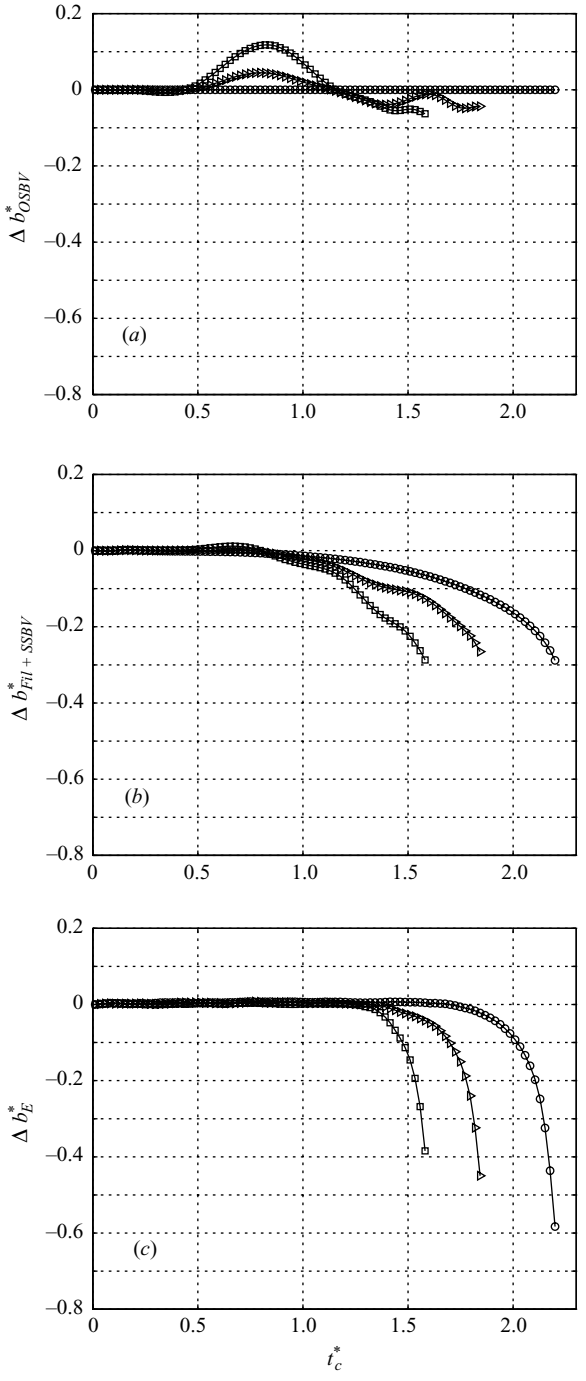

FIGURE 6. Contribution of flow regions to separation distance development, $\Delta b^*_{region}(t)$, for $Re_\Gamma = 5000$, $Fr = \infty, 3, 2$: (*a*) opposite-signed baroclinically generated vorticity (OSBV), (*b*) same-signed baroclinically generated vorticity (SSBV) and filaments, (*c*) exchange band. Symbols: ○, $Fr = \infty$; ▷, $Fr = 3$; □, $Fr = 2$.

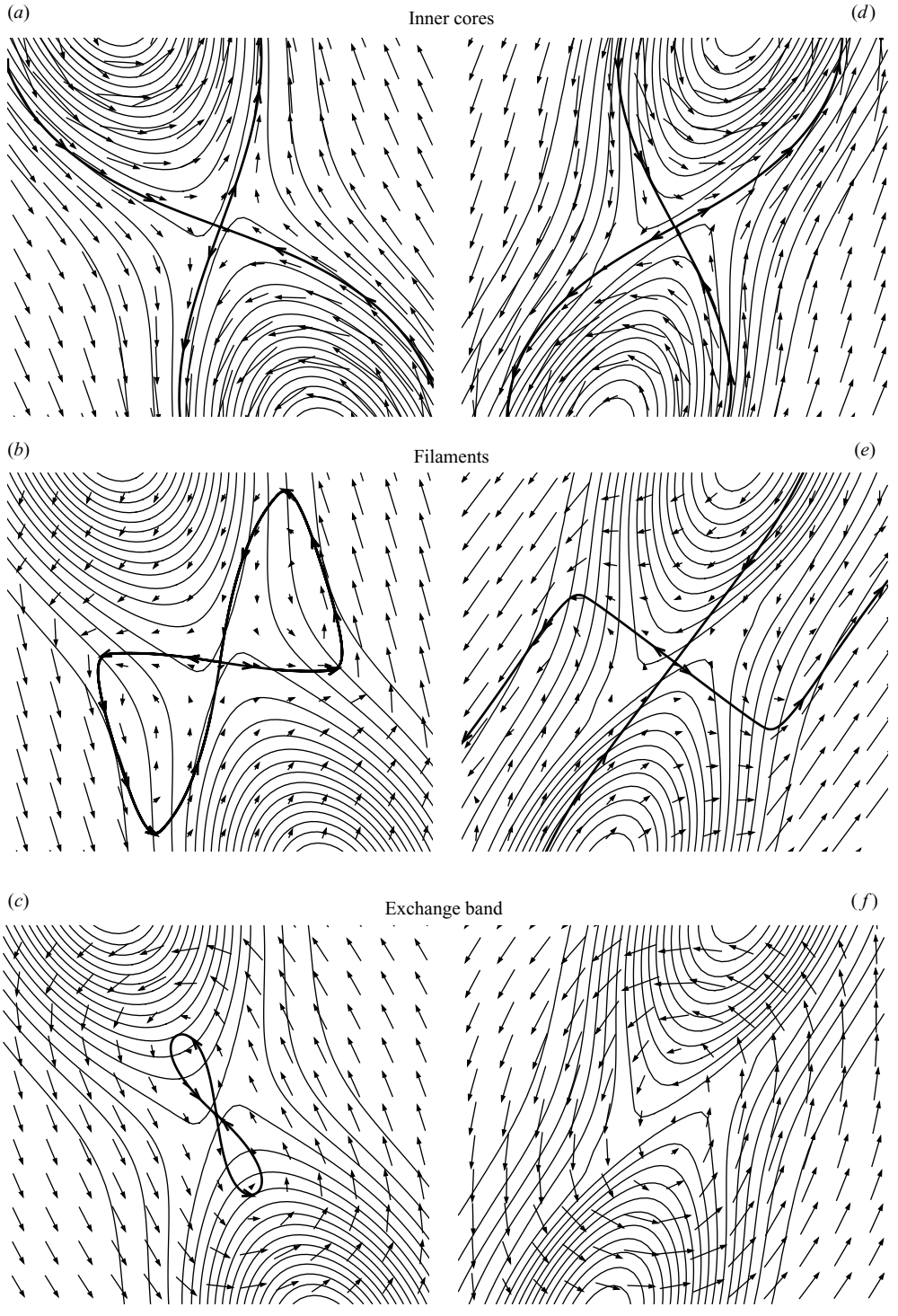

FIGURE 7. Vorticity contours (thin solid lines) superimposed with vectors showing the induced velocity field of the indicated flow regions for $Re_\Gamma = 5000$, $Fr = \infty$ at (*a*)–(*c*) $t_c^* = 1.69$, (*d*)–(*f*) $t_c^* = 1.97$. The heavy solid line represents the induced flow streamline which passes through the centre hyperbolic point. (NB: Inner core and exchange band vector lengths are scaled the same; filament vectors are enhanced an order of magnitude for visibility.)

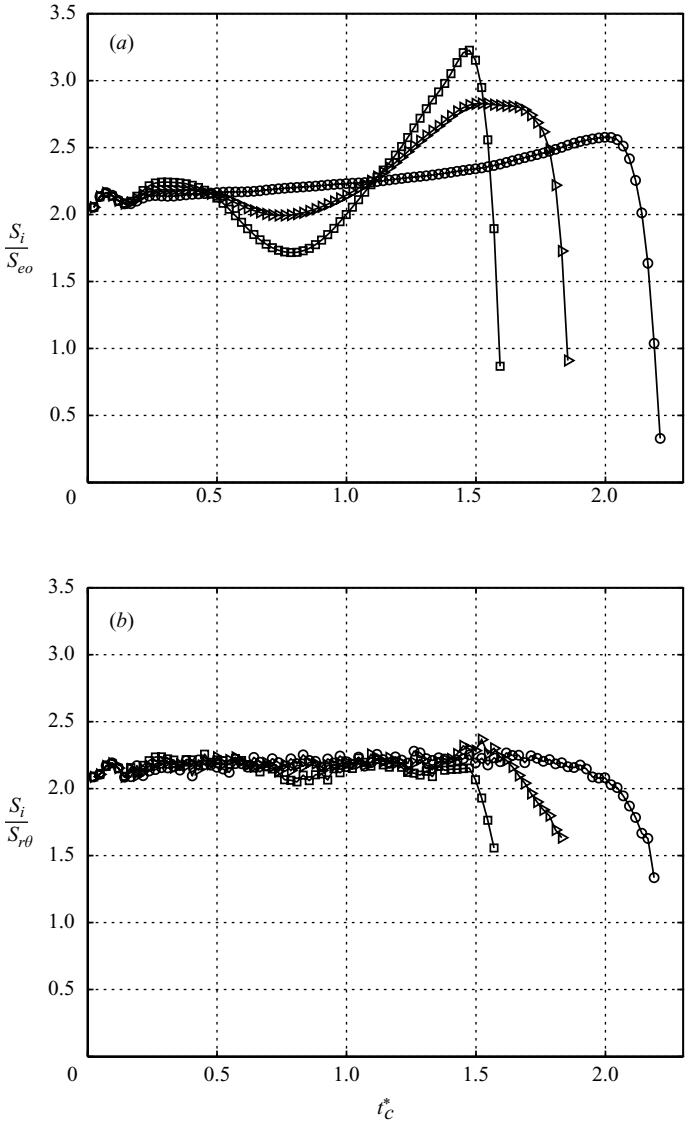

FIGURE 8. Time development of the local strain rate, S_i, at the centre of rotation normalized by the external strain rates (3.4): (*a*) $S_{eo} = S_{r\theta}(b/2, 0)$, (*b*) $S_{r\theta}(b/2, t)$ for $Fr = \infty$, 3, 2, $Re_\Gamma = 5000$. Symbols: ○, $Fr = \infty$; ▷, $Fr = 3$; □, $Fr = 2$.

bands interact and result in a locally enhanced region of strain in the vicinity of the center of rotation (see figure 11*a–c*).

Figure 8*a*, *b* shows the time development of the nondimensionalized local (principal) strain rate evaluated at the center of rotation. As a reference value, we consider the *external* strain at a given location, defined as the strain rate induced by one vortex if the other vortex was not present. The strain field for a Lamb-Oseen vortex (Saffman 1992) is given by

$$S_{r\theta}(r, t) \;=\; \frac{\Gamma_o}{2\pi}\left[-\frac{1}{r^2} + \left(\frac{1}{a^2} + \frac{1}{r^2}\right)\exp\left(-\frac{r^2}{a^2}\right)\right]. \tag{3.4}$$

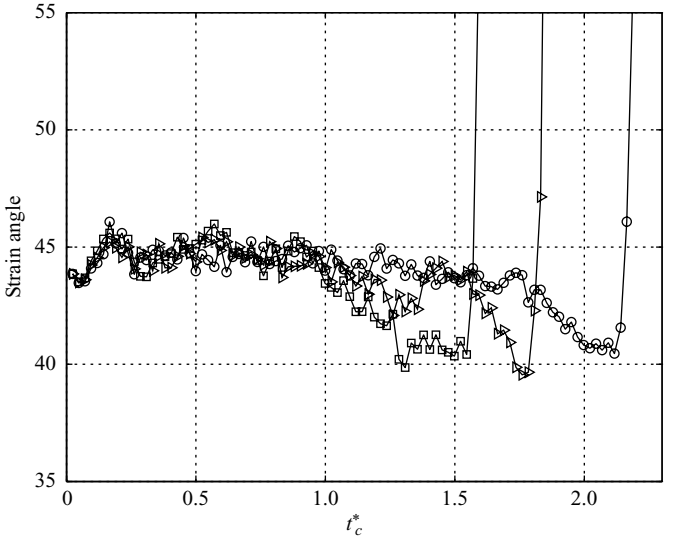

FIGURE 9. Time development of the angle between extensional strain eigenvector and vortex connecting line at the centre of rotation for $Re_\Gamma = 5000$, $Fr = \infty$, 3, 2. Symbols: ○, $Fr = \infty$; ▷, $Fr = 3$; □, $Fr = 2$.

At $t = 0$ (large b/a and $b = b_o$), the external strain value at the center of rotation ($r = b/2$) is $S_{r\theta}(r, 0) = 4\,\Gamma_o/(2\pi {b_o}^2)$. The strain values plotted in figure 8(a) are nondimensionalized by the constant value, $S_{r\theta}(r, 0) = S_{eo}$, and in figure 8($b$) by the time-varying external strain, $S_{r\theta}(r, t)$, which accounts for both $b(t)$ and $a(t)$. Results indicate that the local strain rate for unstratified flow increases linearly during the diffusive phase. Initially the value is approximately twice the external strain, indicating that the contributions from each of the vortices are nearly additive. The main increase during the convective phase is due to the reduction in $b(t)$. This plays a significant role in the merging process in both the unstratified and stratified flows. We note that although $S_{r\theta}(r, t)$ describes the overall behavior quite well for some time, the scaled strain in figure 8(b) does exhibit a slow increase until $t_c^* \sim 1.7$, at which time it decreases and deviates from $S_{r\theta}(r, t)$ significantly. This corresponds to the start of the exchange band process.

The interaction of the vortices will also influence the directionality in $\boldsymbol{S}$, which will in turn affect subsequent vortex deformation (3.5). Figure 9 shows the angle between the extensional strain eigenvector and the vortex connecting line at the center of rotation, i.e. the *relative orientation* of the extensional strain with respect to the vortex pair. At early times in unstratified flow, the angle remains approximately 45° due to the relatively weak interaction between the vortices. At approximately $t_c^* \sim 1.0$, the angle begins to decrease. At $t_c^* \sim 1.7$, the angle is reduced to approximately 43°. At this time, the exchange band process is initiated (figure 6c). Close inspection of the induced flow fields (figure 7a–c), and in particular the streamlines passing through the center hyperbolic point indicating local extensional straining, demonstrates that the exchange band is responsible for the reduction in this angle. Note that the induced flow by the filaments tends to increase this angle (figure 7b). At $t_c^* \sim 2.1$, the angle reaches approximately 40°, beyond which it then rapidly increases. This indicates a substantial change in the flow, i.e. core entrainment, which corresponds to the time $b^*(t)$ begins its rapid and nearly linear descent (figure 5a). The reduction in

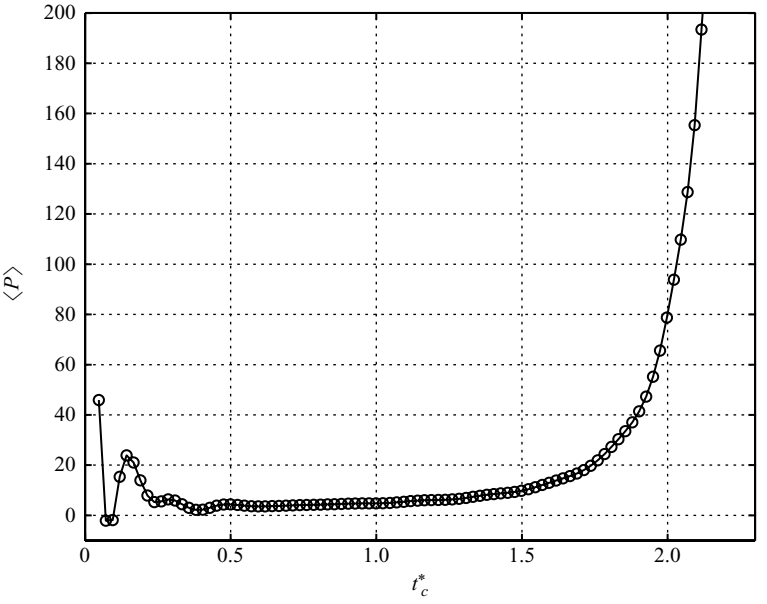

FIGURE 10. Time development of $\langle P \rangle = -\langle \nabla\omega^T \boldsymbol{S} \nabla\omega \rangle$, averaged over domain, for $Re_\Gamma = 5000$, $Fr = \infty$.

strain orientation is associated with the development of the tilt in ω contours (see figure 11*a–c*). We will consider this angle as an indicator of the tilt, which results from a dynamic interaction between vorticity and strain.

In a two-dimensional flow, the interaction of ω and $\boldsymbol{S}$ is understood in terms of the vorticity gradient, $\nabla\omega$, which may undergo reorientation and amplification by $\boldsymbol{S}$. It is directly related to the behavior of vorticity contours since $-\nabla\omega/|\nabla\omega|$ is the local normal vector of an isovorticity contour line. The equation for $|\nabla\omega|^2$ in unstratified flow is

$$\frac{\mathrm{D}\frac{1}{2}|\nabla\omega|^2}{\mathrm{D}t} = |\nabla\omega|^2 \frac{\mathrm{D}\ln|\nabla\omega|}{\mathrm{D}t} = -\nabla\omega^T \boldsymbol{S} \nabla\omega + \nu \nabla\omega^T \nabla^2 \nabla\omega. \tag{3.5}$$

The two terms on the right-hand side represent gradient amplification and diffusion, respectively. Here, we define two quantities associated with the production term: $P = -\nabla\omega^T \boldsymbol{S} \nabla\omega$ and $P_s = -(\nabla\omega^T \boldsymbol{S} \nabla\omega)/|\nabla\omega|^2$ (P_s obtained by dividing (3.5) by $|\nabla\omega|^2$), whose sign indicates the relative orientation of $\nabla\omega$ with the principal strain axes and, in the case of P_s, the magnitude indicates the strain in the direction of $\nabla\omega$. Thus, P, $P_s > 0$ correspond to $\nabla\omega$ orienting towards the direction of the compressive strain, i.e. there is gradient amplification by compressive straining. Figure 10 shows the time development of the area-averaged production term, $\langle P \rangle$, which indicates a global mean rate of deformation of the vorticity field. Prior to merging, the behavior of $\langle P \rangle$ is consistent with the elliptic deformation of the vortices as characterized by computed eccentricities (not shown). As discussed in Le Dizes & Verga (2002), beyond the initial flow adjustment and prior to the merging threshold, the vortices relax to a mean state in which they deform at a steady rate. This mean state corresponds to the small and nearly constant value exhibited by $\langle P \rangle$ during this time (figure 10). A net positive value of $\langle P \rangle$ is exhibited, indicating the significance of the gradient

amplification process. Beyond the diffusive phase, there is a significant increase in $\langle P \rangle$, indicating deviation from the mean state and accelerated deformation.

In general, the local behavior of P will depend on the relative significance of rotation and strain. In rotation-dominated regions ($II > 0$), P oscillates between positive and negative values. Physically, $\nabla\omega$ rotates and alternates between amplification and damping, a condition which results in elliptic instability (Protas, Babiano & Kevlahan 1999). We expect the *dynamic* effect of P on $\nabla\omega$ to be most significant in strong strain-dominated regions ($II < 0$), i.e. the exchange band region, and in particular in the vicinity of the center of rotation, where there is an enhancement of strain. In these regions, $\boldsymbol{S}$ is dynamically active and significantly alters $\nabla\omega$.

Figure 11 shows $\boldsymbol{S}$ (vectors) and P_s (light gray scale, $P_s > 0$; dark gray scale, $P_s < 0$) superimposed on vorticity contours at the central region of the vortex pair at three times. Each vortex exhibits the quadrupole structure of P associated with elliptic vortices (Kimura & Herring 2001). As discussed in Kimura and Herring, in positive P_s (compressive straining) regions ω isocontours are squeezed together, while at the same time they are extended in the orthogonal direction due to flow incompressibility. The opposite is true for negative P_s regions. This is seen in figure 11(e) where, in the vicinity of the center (hyperbolic point) and above it, ω contours in $P_s > 0$ regions extend to the left, while ω contours in $P_s < 0$ regions contract to the left. This results in the observed tilting of the upper vortex to the left and a corresponding tilting of the lower vortex to the right, which thereby tilts the vortices with respect to their connecting line (Brandt & Nomura 2006). This also results in the central region to be dominated by $P_s > 0$, i.e. gradient amplification. The tilting effect also occurs in the vicinity of the outer hyperbolic points where filamentation initiates (not shown). In their study of isolated elliptic vortices, Kimura & Herring (2001) show that P plays a significant role in the filamentation process. In regions of $P > 0$, vorticity gradient amplification was found to occur prior to filament ejection. This is also observed in the present case of two co-rotating vortices.

As discussed by Le Dizes & Verga (2002), prior to merging, the vorticity and streamfunction exhibit a distinct functional relation, suggesting that the flow in the rotating frame is nearly a stationary solution to the Euler equation. However, in time and near the merging threshold, the relation between ω and the streamfunction deviates at the hyperbolic points where $|\omega|$ is low (see their figure 14). At the central hyperbolic point, they find an accumulation of vorticity and a Reynolds number dependence which they suggest is due to complex advection–diffusion processes. Based on our results, we conclude that the tilt of the vortices and associated diffusion, which is enhanced by gradient amplification ($P_s > 0$ at center), results in this accumulation and the observed misalignment of ω contours with respect to the streamlines in these regions (e.g. figure 7*a*). Since the streamlines are separatrices, this causes vorticity to enter a different flow region in the co-rotating frame and be advected away.

In order to examine further the development of the tilt, we define the *central region* of the flow by a box in the co-rotating frame with a width of $0.25b_o$ (along the connecting line of the vortices) and a height of $0.08b_o$. The box dimensions are chosen to capture the primary misalignment in ω contours. Figure 12 shows $\langle P \rangle$ averaged over the central region which is predominantly positive and exhibits a significant increase beyond $t_c^* \gtrsim 0.5$. This increase corresponds directly to the extension of $P_s > 0$ regions and the positive feedback nature of gradient amplification by compressive straining. Since the production term, $\nabla\omega^T \boldsymbol{S} \nabla\omega$, depends on both the magnitudes and relative orientation of $\nabla\omega$ and $\boldsymbol{S}$, we now isolate the directional component.

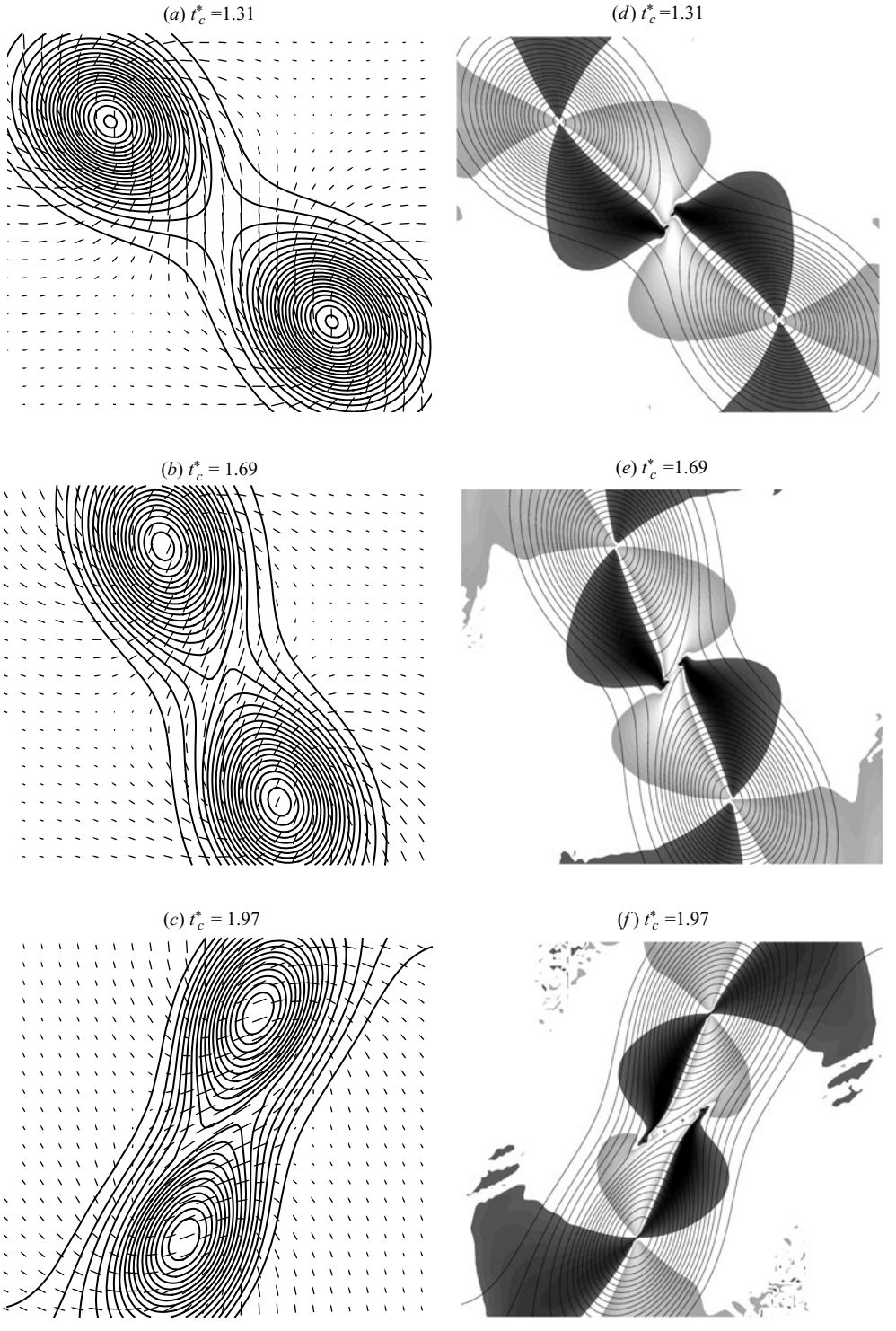

FIGURE 11. Close-up of vorticity contours with (*a*)–(*c*) superimposed principal extensional strain (vectors indicating magnitude of eigenvalue and direction of eigenvector), (*d*)–(*f*) grey shading corresponding to $|\nabla\omega|^2$ production term, $P_s = -(\nabla\omega^T \mathbf{S}\nabla\omega)/|\nabla\omega|^2$ (light grey scale, $P_s > 0$; dark grey scale, $P_s < 0$), for $Re_\Gamma = 5000$, $Fr = \infty$.

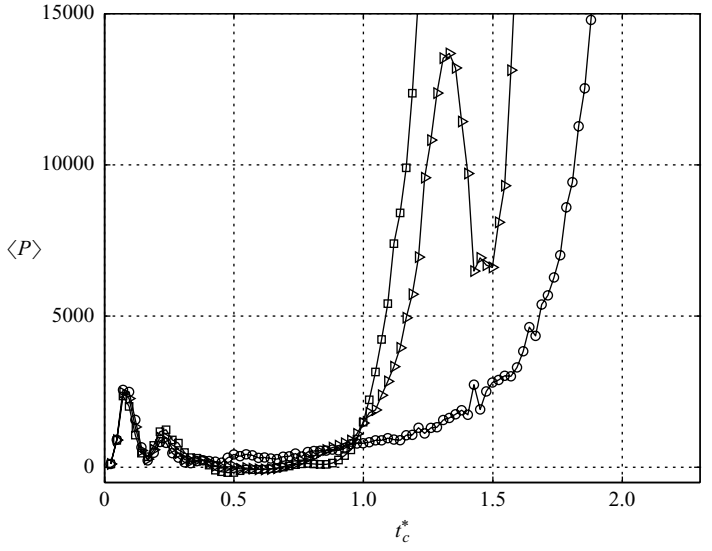

FIGURE 12. Time development of $\langle P \rangle = -\langle \nabla\omega^T \boldsymbol{S} \nabla\omega \rangle$ in the central region for $Re_\Gamma = 5000$. Symbols: ○, $Fr = \infty$; ▷, $Fr = 3$; □, $Fr = 2$.

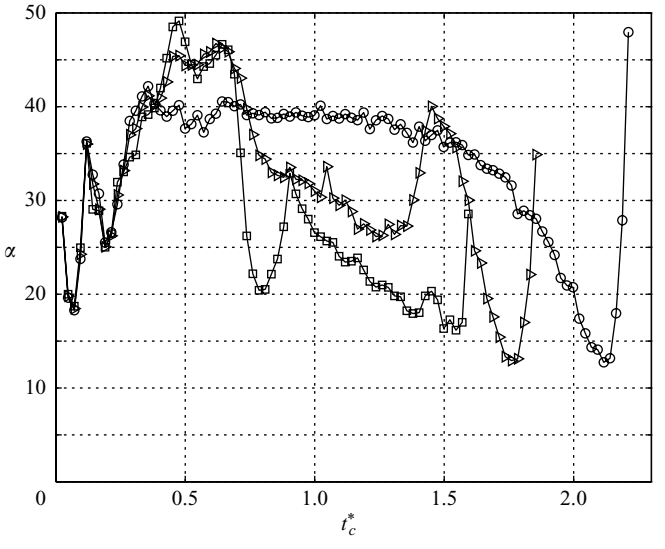

FIGURE 13. Time development of the angle between $\nabla\omega$ and compressive strain, α, in the central region for $Re_\Gamma = 5000$, $Fr = \infty, 3, 2$. Symbols: ○, $Fr = \infty$; ▷, $Fr = 3$; □, $Fr = 2$.

Figure 13 shows the average angle between $\nabla\omega$ and the compressive strain eigenvector in the central region. Beyond the initial adjustment period in the unstratified flow, the average angle is $\sim 40°$, which is near the 45° associated with a *passive* strain field, i.e. controlled by the primary vortex. Beyond a time $t_c^* \sim 1$, the angle decreases towards zero, indicating that the strain has become *active* in influencing the vorticity field by amplifying and reorienting $\nabla\omega$. This corresponds to the development of the tilt (figure 9). As observed in these figures, significant differences occur in the stratified flows. These will be explained in § 3.4.

In summary, we present the following description of the merging process, which we consider to consist of *four* phases. During the *diffusive/deformation phase*, $b^*(t)$ remains constant and the vortices grow by diffusion. The induced strain field of each of the vortices correspondingly spreads by diffusion and also develops through their mutual interaction. In the strain-dominated regions of the flow, and in particular in the vicinity of the center hyperbolic point where the mutual interaction of strain is strongest, $\boldsymbol{S}$ becomes dynamically active and influences the vorticity field through amplification and reorientation of $\nabla\omega$. This establishes a tilt in ω contours with respect to the vortex connecting line which, together with diffusion, results in a misalignment of ω with respect to the streamlines. At the outer regions of the exchange band (near outer hyperbolic points), this causes ω to enter the outer-recirculation region and filamentation to occur. The associated vorticity acts to advect the vortices towards each other but does not drive the merger to completion. We consider this as the *convective/deformation phase* since the (slow) reduction in $b^*(t)$ enhances the induced strain at the vortices and central region. In the vicinity of the center hyperbolic point, this misalignment allows inner core ω to enter the exchange band and be advected away from its source core. This is the start of the *convective/entrainment phase*, which is associated with a rapid reduction in $b^*(t)$. The inner cores are thereby stripped and eroded. The circulation of the exchange band increases at the expense of that of the inner cores, which become increasingly weak. At some point, the cores themselves are entrained. The resulting fluid motion becomes rotation-dominated, and what is essentially a single vortex is established. The last phase, *diffusive/axisymmetrization phase*, is characterized by the final slow reduction in $b^*(t)$ as the two ω maxima diffuse and the flow evolves towards axisymmetry.

As will be discussed in the following sections, this new description of merger, which resolves the convective phase into the two distinct processes, assists in accounting for the effects of stratification and allows for a more explicit determination of the critical aspect ratio.

3.3. *Baroclinic torque generation*

We first consider the basic physics of the stratified flow. As observed in figure 4, additional vorticity develops in the flow. As the vortex pair rotates, it stirs the stably stratified ambient fluid and establishes horizontal density gradients, $\partial\rho'/\partial x$, which generates vorticity through baroclinic torque, as described by the last term in the vorticity equation for two-dimensional flow,

$$\frac{\partial\omega}{\partial t} + (\boldsymbol{v}\cdot\nabla)\omega \;=\; \nu\nabla^2\omega \;-\; \frac{1}{\rho_o}\nabla\rho' \times g\boldsymbol{k}. \tag{3.6}$$

Plots are presented showing vorticity contours superimposed on the associated baroclinic torque (figure 14) for $Fr = 3$ at the same times given in figure 4.

As indicated in figure 4, after approximately a quarter-rotation and then another half-rotation beyond (figure 4*a–c*, $t_c^* = 0.26 - 0.78$), the vortex pair establishes significant $\partial\rho'/\partial x$ at its periphery, thereby resulting in negative baroclinic torque on the left and right sides of the pair (figure 14*a–c*). As indicated at the later time (figures 4*c*, 14*c*; $t_c^* = 0.78$), this results in *opposite-signed baroclinically generated vorticity*, OSBV, which forms at the boundary of the outer-recirculation regions. After three-quarters rotation ($t_c^* = 0.78$), we also observe significant $\partial\rho'/\partial x$ at the periphery of the primary cores due to fluid that is entrained into the outer recirculation regions (figures 4). The presence of this entrained fluid leads to a layer of *same-signed baroclinically generated vorticity*, SSBV, just inside the previous OSBV after the

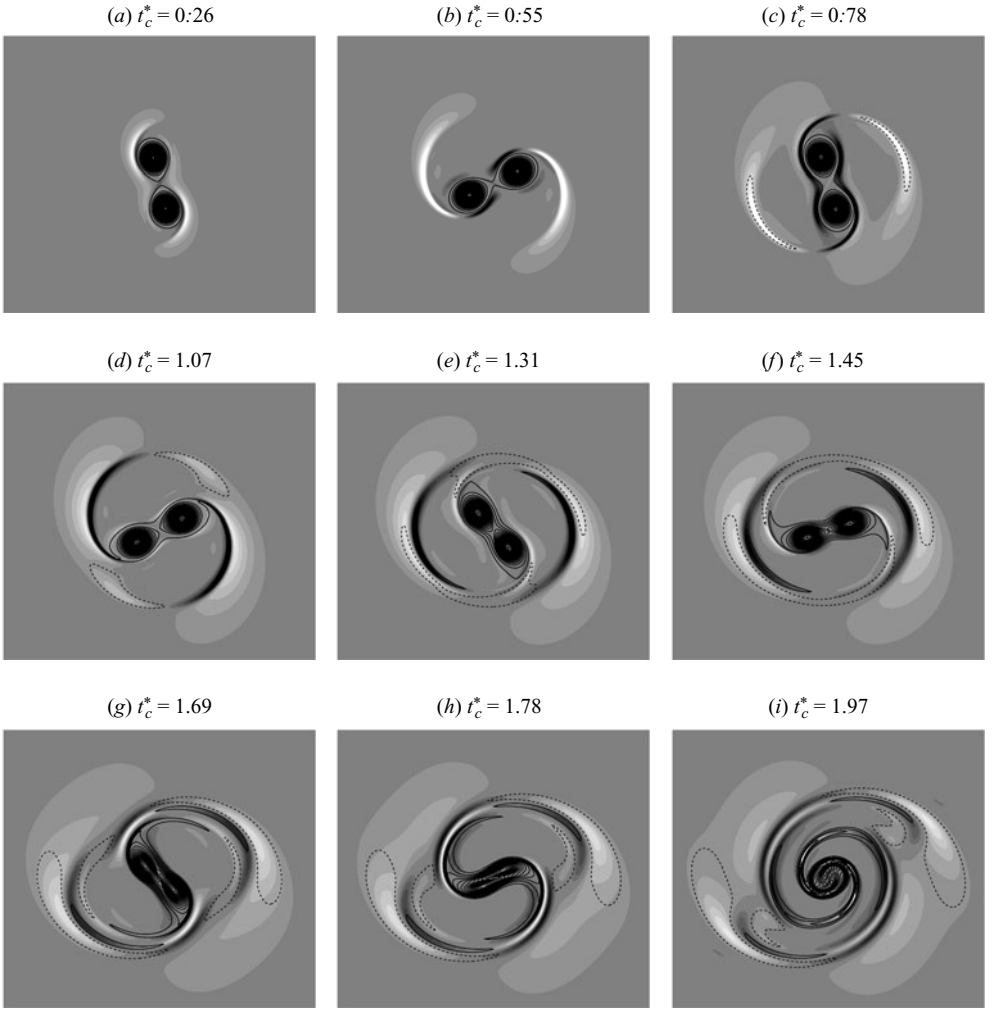

FIGURE 14. Vorticity contours (lines) superimposed on baroclinic torque, $-\nabla\rho' \times g\boldsymbol{k}/\rho_o$ (dark shading, positive; light shading, negative), for $Re_\Gamma = 5000$, $Fr = 3$.

completion of one full revolution (figures 4*d*, 14*d*; $t_c^* = 1.07$). The SSBV is extended as the vortex pair continues its rotation, thereby establishing same-signed ω, filament-like structures (figures 4*e*, 14*e*; $t_c^* = 1.31$). Note that filamentation of primary ω is also occuring. This is observed in the vorticity contours in figures 4*f*, *g* and 14*f*, *g*, in which ω from the primary cores is entering into the outer-recirculation region. At later times, continued stirring of ρ results in successive generation of $\partial\rho'/\partial x$, resulting in layers of alternate-signed baroclinic torque (figure 14*i*, $t_c^* = 1.97$).

3.4. *Vortex merging: stratified flow*

As indicated in figure 5(*a*), merging is completed earlier in stratified flows, although $b^*(t)$ exhibits a more complex development. The contributions to the change in b^* of each of the flow regions are shown in figure 6. Here, the outer-recirculation region is subdivided into two regions: (*a*) OSBV and (*b*) filaments and SSBV (i.e. same-signed $\boldsymbol{\omega}$ is considered together).

The OSBV (figure 6*a*) causes the vortices initially to move apart after half a rotation ($t_c^* \sim 0.5$). After $t_c^* \sim 0.78$, the vortices then move together until $t_c^* \sim 1.45$, approximately half a revolution later, at which time they begin to move apart again. As observed in figures 4 and 14, OSBV forms arches at the lower left and upper right peripheral regions that are nearly stationary as the vortex pair rotates. The resulting spatial distribution causes the induced motion to vary with the rotation as described. Beyond the first complete revolution, the behavior is more complex as additional layers of OSBV are formed (figures 14, 6; $t_c^* > 1.45$). With increased stratification ($Fr = 2$), the magnitudes of OSBV are greater, thereby increasing the amplitude of the corresponding induced velocity and contribution to $b^*(t)$. However, the frequency of the contribution is unchanged since baroclinic torque depends on the rotation of the vortex pair.

The SSBV, together with the filaments (figure 6*b*), contributes to a decrease in b^*. The induced motion of same-signed ω in the outer-recirculation region is initiated at nearly the same time ($t_c^* \sim 1$) in both the stratified and unstratified flows. However, the presence of the additional vorticity, i.e. the SSBV, enhances the motion and thereby the *rate of decrease* in $b^*(t)$, the effect being stronger with increased stratification ($Fr = 2$). The exchange band contribution (figure 6*c*) occurs earlier in time in the stratified flows. From the vorticity contour plots for $Fr = \infty$ and $Fr = 3$ flows (figures 3*d*, 4*d*; $t_c^* = 1.07$), we see that a slight tilt in the lowest-level ω contour near the origin appears at an early time in both flows. At the subsequent time (figures 3*e*, 4*e*; $t_c^* = 1.31$), the tilt is diminished in the unstratified flow while it is maintained in the stratified flow. This causes the exchange band process to proceed earlier in time. From figure 6(*c*), we see that while the exchange band process in stratified flows initiates earlier than in unstratified flow, the slope of the rapid decrease is not significantly altered by stratification, indicating that the same physics is associated with this process, i.e. core entrainment is not significantly influenced by stratification in the considered flows.

Figure 15 shows the induced flow fields of the OSBV and the filaments and SSBV for the $Fr = 3$ flow. The OSBV-induced flow (figure 15*a–c*) resembles that of the filaments, but exhibits a cyclic behavior with respect to its direction, consistent with the results in figure 6(*a*). As the plotted streamlines indicate, this influences both the magnitude and the relative orientation of the strain rate in the vicinity of the center of rotation. The flow induced by the filaments and SSBV combined (figure 15*d–f*) is similar to that of only filaments in unstratified flow (figure 7*b*, *e*). The induced flow by the exchange band (not shown) is similar to that of unstratified flow (figure 7*c*, *f*). Note that although the tilt in ω contours is established earlier in time ($t_c^* = 1.31$), a reduction in the tilt is observed at a later time ($t_c^* = 1.45$) in this flow. This is also indicated by the strain orientation in figure 9.

The development of the tilt in the ω contours is now considered. The equation for $|\nabla\omega|^2$ in stratified flow is

$$\frac{\mathrm{D}\frac{1}{2}|\nabla\omega|^2}{\mathrm{D}t} = -\nabla\omega^T \boldsymbol{S} \nabla\omega + \nu\nabla\omega^T\nabla^2\nabla\omega + \frac{1}{\rho_o}\nabla\omega^T\nabla(\nabla\rho' \times \boldsymbol{g}), \tag{3.7}$$

in which there is an additional term associated with the gradient of baroclinic torque. However, in the central region of the flow, it is not expected to be significant in comparison with P, and evaluation of this term confirms this. Figure 16 shows the P_s field for the $Fr = 3$ flow. At $t_c^* = 1.31$ (figure 16*a*), we observe the same basic features as in the unstratified flow (figure 11); however, higher values of $P_s > 0$ are

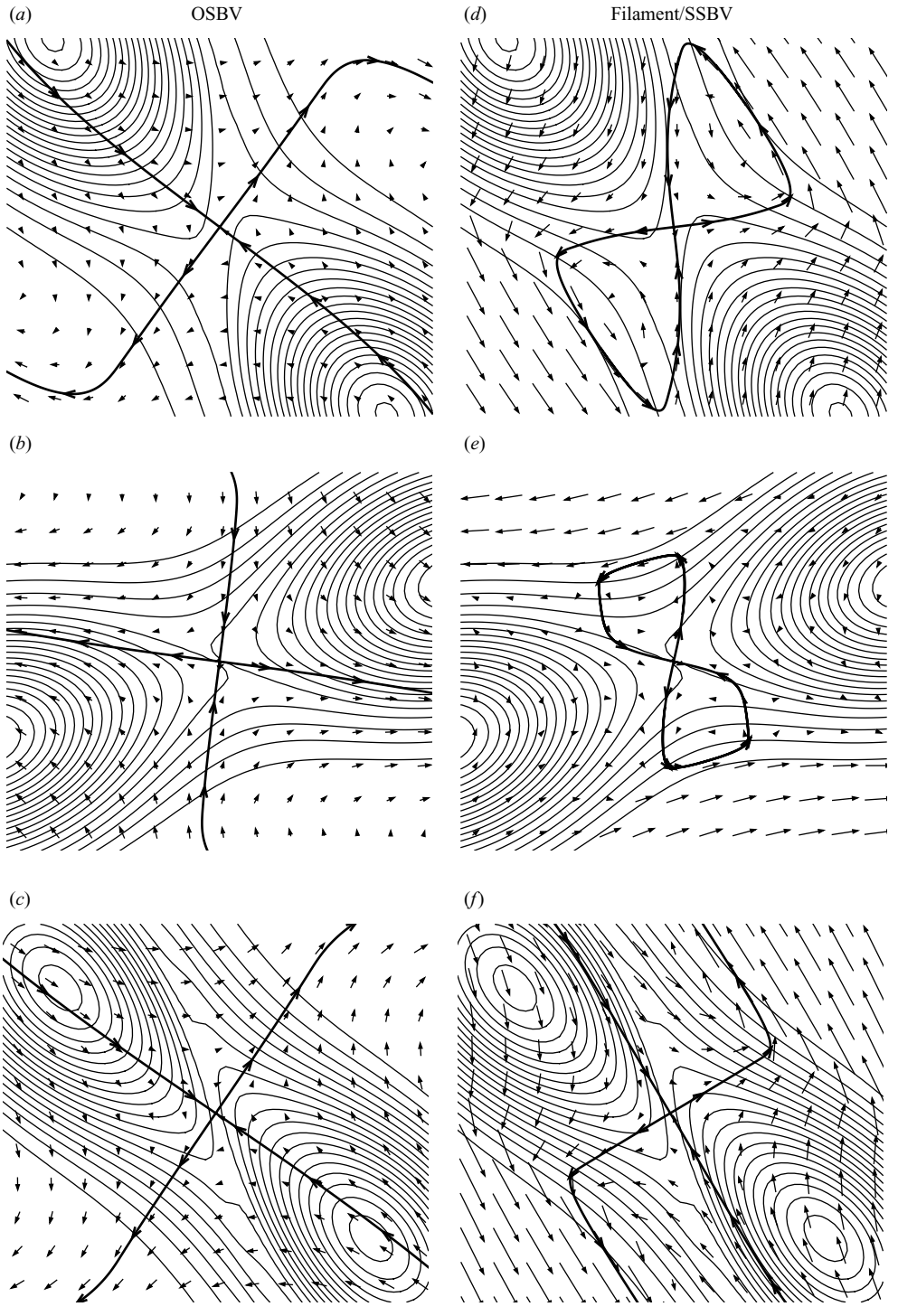

FIGURE 15. Vorticity contours (thin solid lines) superimposed with vectors of the induced velocity field of OSBV (on the left) and Filament/SSBV (on the right) for $Re_\Gamma = 5000$, $Fr = 3$ at (*a*), (*d*) $t_c^* = 1.31$, (*b*), (*e*) $t_c^* = 1.45$, (*c*), (*f*) $t_c^* = 1.69$. The heavy solid line represents the induced flow streamline which passes through the centre hyperbolic point. (NB: The filament/SSBV vector lengths are on the same order of magnitude as in figure 7. The OSBV vectors are enhanced an order of magnitude for visibility.)

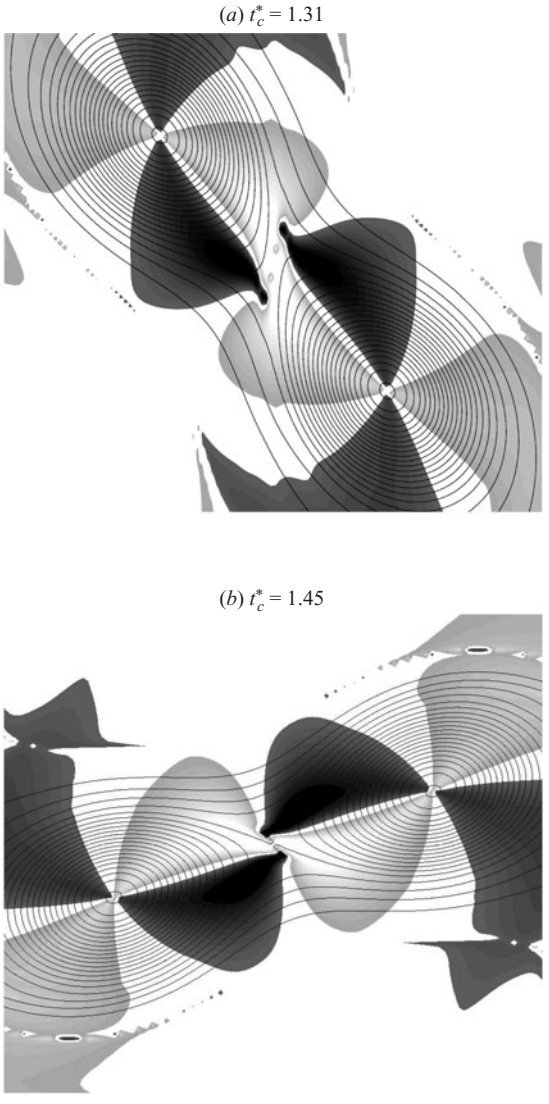

FIGURE 16. Vorticity contours with grey shading corresponding to $|\nabla\omega|^2$ production term, $P_s = -(\nabla\omega^T \mathbf{S}\nabla\omega)/|\nabla\omega|^2$ (light grey scale, $P_s > 0$; dark grey scale, $P_s < 0$), for $Re_\Gamma = 5000$, $Fr = 3$, (*a*) $t_c{}^* = 1.31$, (*b*) $t_c{}^* = 1.45$.

observed, consistent with the establishment of the tilt at this earlier time. At $t_c^* = b1.45$ (figure 16*b*), there is an enhancement of regions of $P_s < 0$ in the central region associated with the reduction in the tilt. The time development of $\langle P \rangle$ for the central region is given in figure 12. In the stratified flows, a slight decrease to negative values is observed at $t_c^* \sim 0.5$ followed by an increase to predominantly positive values for $t_c^* > 0.75$. For $t_c^* > 1$, the rate of increase in $\langle P \rangle$ is greater than that of the unstratified flow. This results in the earlier development of the tilt and subsequent exchange band process. Note that there is a marked difference between the two stratified cases. In the $Fr = 3$ flow, $\langle P \rangle$ exhibits a sharp dip, while in the $Fr = 2$ flow, $\langle P \rangle$ continues to increase. The reduction in $\langle P \rangle$ for $Fr = 3$ corresponds with the observed reduction in tilt (figure 16*b*; $t_c^* = 1.45$). Beyond $t_c^* \sim 1.5$, $\langle P \rangle$ resumes its rapid increase.

The behaviour of $\langle P \rangle$ is explained by considering both the magnitude and orientation of $\boldsymbol{S}$. Time development of the local strain rate at the center of rotation is shown in figure 8(a) and indicates a reduction in magnitude during $0.5 < t_c^* < 0.78$, followed by an increase until $t_c^* \sim 1.5$. Prior to core entrainment, the induced strain is directly related to changes in the separation distance and generally follows (3.4) as indicated by figure 8(b). As the vortices move away from each other due to the OSBV ($0.5 < t_c^* < 0.78$), the strain at the center of rotation is reduced, and as they move towards each other ($0.78 \lesssim t_c^* \lesssim 1.35$), the strain is increased; the effect of OSBV on $\langle P \rangle$ is cyclic. Beyond $t_c^* \sim 1.35$ the OSBV has less of an effect, particularly in the $Fr = 2$ flow. This may be attributed to the greater extent of OSBV surrounding the vortex pair, which results in some effective cancellation of the associated flow. Since the SSBV acts only to reduce $b^*(t)$, SSBV enhances the strain, thereby resulting in higher strain in the stratified flows than that of the unstratified flow for $t_c^* > 1.1$ (figure 8a). Thus, the effect of SSBV is to promote $\langle P \rangle$. In the $Fr = 2$ flow, the strain magnitude continues to increase due to the OSBV, SSBV and exchange band induced flows until it exhibits a sharp drop due to core entrainment, which occurs earlier in time. In the $Fr = 3$ flow, while the SSBV enhances the strain, its induced radial velocity is much smaller than in the $Fr = 2$ flow and the OSBV counteracts this effect. The reduction in $b^*(t)$ is thereby delayed during $1.35 \lesssim t_c^* \lesssim 1.55$. Beyond this, the strain magnitude levels off before it drops as core entrainment occurs (figure 8a). This does not, however, fully explain the observed reduction in tilt at $t_c^* \sim 1.45$ in the $Fr = 3$ flow.

As indicated earlier, the induced flows (figure 15) also influence the orientation of $\boldsymbol{S}$. As shown in figure 9, the orientation angle of the extensional strain at the center of rotation begins to decrease from 45° at approximately $t_c^* \sim 1$ and does so at a greater rate in the stratified flows than in the unstratified flow. Examination of figure 15(a)–(c) indicates that the induced flow of the OSBV rotates with respect to the vortex connecting line and thus has a cyclic influence on the strain rate orientation. In the $Fr = 3$ flow, for $1.0 \lesssim t_c^* \lesssim 1.35$, the induced flow enhances the reduction in the strain orientation angle, while for $1.35 \lesssim t_c^* \lesssim 1.55$ it opposes the reduction. This explains the observed increase in the angle at $t_c^* \sim 1.45$ (figure 15b, e). The reduction in $\langle P \rangle$ during this time (figure 12b, e) and corresponding reduction in the tilt is associated with a reduced alignment between $\nabla\omega$ and the compressive strain (figure 13). However, beyond this time, the angle resumes its decrease until core entrainment occurs, at which point the strain angle sharply diverges as the flow becomes vorticity-dominated. In both stratified flows, the rotation of the strain axes is such as to generally promote the alignment of the compressive strain and $\nabla\omega$, thereby increasing P and enhancing the gradient amplification process. As illustrated by this process, the interaction of $\nabla\omega$ and $\boldsymbol{S}$ is complex. While local $\boldsymbol{S}$ interacts directly with $\nabla\omega$, through both its magnitude and relative orientation, both local and nonlocal ω will feed back on $\boldsymbol{S}$.

In summary, we describe vortex merging in the stratified flows in terms of the four phases of development presented in § 3.2. This is illustrated in figure 17. The diffusive/deformation phase begins as in unstratified flow; however, it is interrupted by an earlier convective/deformation phase due to baroclinically generated vorticity. Essentially, the OSBV and SSBV play a similar role to that of the filaments, i.e. the induced flow advects the vortices, thereby modifying $\boldsymbol{S}$, which in general may hinder or enhance the gradient amplification process. In the flows considered, the combined effects of the enhanced magnitude and change in orientation of $\boldsymbol{S}$ by OSBV and SSBV leads to a more rapid development of the tilt in ω contours and subsequent exchange

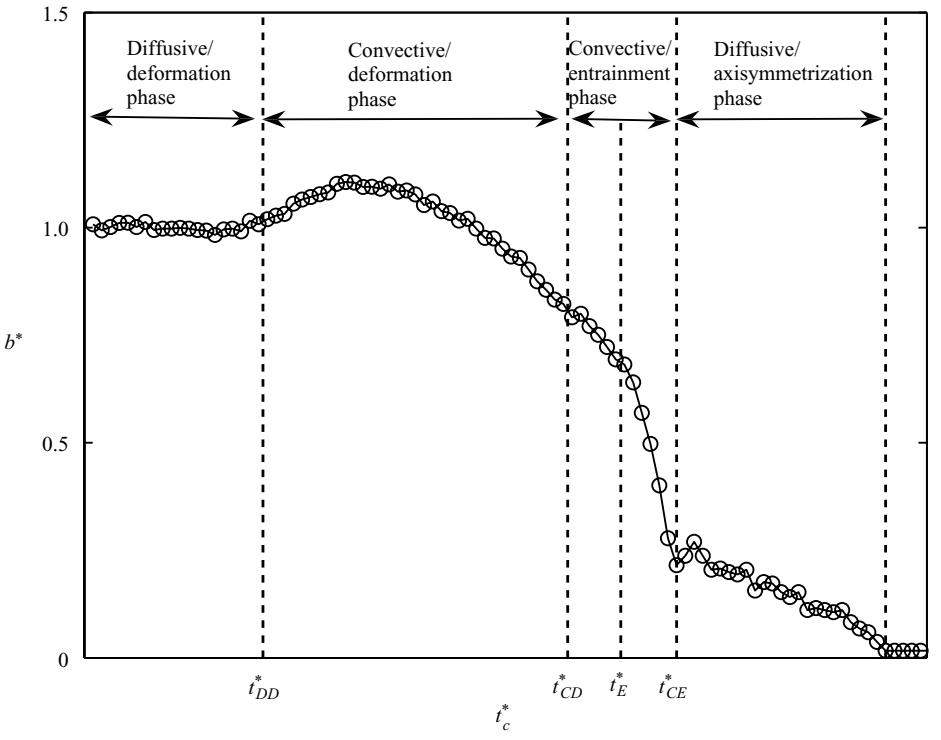

FIGURE 17. Diagram illustrating four phases of merging process with respect to the development of $b^*(t)$ for $Re_\Gamma = 5000$, $Fr = 2$ ($t^*_{DD} = 0.49$, $t^*_{CD} = 1.32$, $t^*_E = 1.46$, $t^*_{CE} = 1.62$).

band process. In general, the effects of both OSBV and SSBV depend on the rotation of the vortex-pair and are cyclic. Thus, their implication on the merging process will depend on the relative time and stage of flow development that they appear. This issue will be considered in the following section. Once the core entrainment process is initiated, the convective/entrainment phase proceeds as in the unstratified flow.

3.5. *Flow development and the effect of* Re_Γ

We have developed a description of the vortex-merging process in both unstratified and stratified flows in terms of four phases of development (figure 17) based on results for $Re_\Gamma = 5000$. We now further develop this description by more explicitly defining and delimiting the phases. In particular, we consider the determination of the critical aspect ratio. We also generalize the description for stratified flows by considering the effect of Re_Γ.

During the diffusive/deformation phase ($t^*_c < t^*_{\mathrm{DD}}$), $a^2_\theta(t)$ grows linearly by diffusion while $b(t)$ remains constant. As indicated in figure 5(b), the growth of $a^2(t)$ is well described by (3.3) and the average growth rate for all our simulations, $2000 \leqslant Re_\Gamma \leqslant 5000$ and $Fr = \infty$, 5, 3, 2, is $c' = 1.94 \pm 0.05$. Physically, as the vorticity distribution spreads by diffusion, the induced strain field of each of the vortices correspondingly spreads and develops through their mutual interaction. The vortices adjust to the induced strain, which results in deformation of the vorticity field. Thus, the interaction of $\nabla\omega$ and $\boldsymbol{S}$ is established by diffusion. This is indicated in figure 18, which shows the development of $\langle P \rangle$ plotted against time scaled by the diffusive time

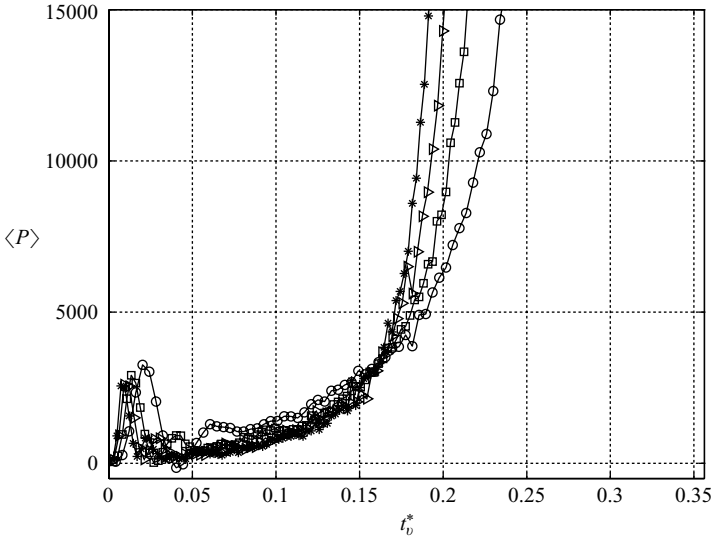

FIGURE 18. Time development of $\langle P\rangle = -\langle \nabla\omega^T \boldsymbol{S} \nabla\omega\rangle$ over central region for $Fr = \infty$ flows. Symbols: ○, $Re_\Gamma = 2000$; □, $Re_\Gamma = 3000$; ▷, $Re_\Gamma = 4000$; ∗, $Re_\Gamma = 5000$.

scale, t_v^*,

$$t_v^* = \frac{t}{t_v} = \frac{t_c}{t_v}\frac{t}{t_c} = \frac{8\pi^2}{(a_o/b_o)^2 Re_\Gamma} t_c^*, \tag{3.8}$$

for the unstratified flows at different Re_Γ. The diffusion rate of ω and $\boldsymbol{S}$ is higher for lower Re_Γ and the initial interaction is established earlier. Beyond the initial rapid adjustment from initial conditions, the behavior of $\langle P\rangle$ generally scales well with t_v^* until $t_v^* \sim 1.1$ (figure 18). Beyond this time, convective effects become important and the higher Re_Γ flows exhibit a greater rate of increase in $\langle P\rangle$.

During the convective/deformation phase ($t_{\mathrm{DD}}^* \leqslant t_c^* < t_{\mathrm{CD}}^*$), $a_\theta^2(t)$ continues to grow linearly and $b(t)$ changes by advection. In unstratified flow, the change in $b^*(t)$ is due to filamentation. The induced flow by the filaments causes a relatively slow reduction in $b^*(t)$ and thus $(a/b_o)_{cr}$ will vary only slightly with Re_Γ. At the end of the convective/deformation phase, $t_c^* = t_{\mathrm{CD}}^*$, and $a_\theta^2(t)$ deviates from linear growth at $(a/b_o)_{cr} \sim 0.23$ (e.g. figure 5*c*) which we find to be nearly independent of Re_Γ. In stratified flow, OSBV and SSBV, together with the filaments, cause $b^*(t)$ to vary more significantly during the convective/deformation phase. The induced flow from OSBV and SSBV may advect the vortices, either away from or towards each other, thereby modifying $\boldsymbol{S}$ and hindering or enhancing, respectively, the development of the tilt in ω contours. In the stratified flows presented in § 3.4, a greater rate of decrease in $b^*(t)$ leads to an earlier start of the exchange band process. However, in general, the effects of OSBV and SSBV may also separate the vortices, i.e. the merger process may, to some extent, be reversed. We therefore distinguish this convective process explicitly by this phase.

During the convective/entrainment phase ($t_{\mathrm{CD}}^* \leqslant t_c^* < t_{\mathrm{CE}}^*$), $a_\theta^2(t)$ no longer grows linearly (the ω field is significantly altered) and $b(t)$ significantly decreases as the vortex cores are eroded and entrained into the exchange band. In contrast to the convective/deformation processes, we consider erosion and entrainment to be irreversible. We now define the critical state of the flow to be the start of the

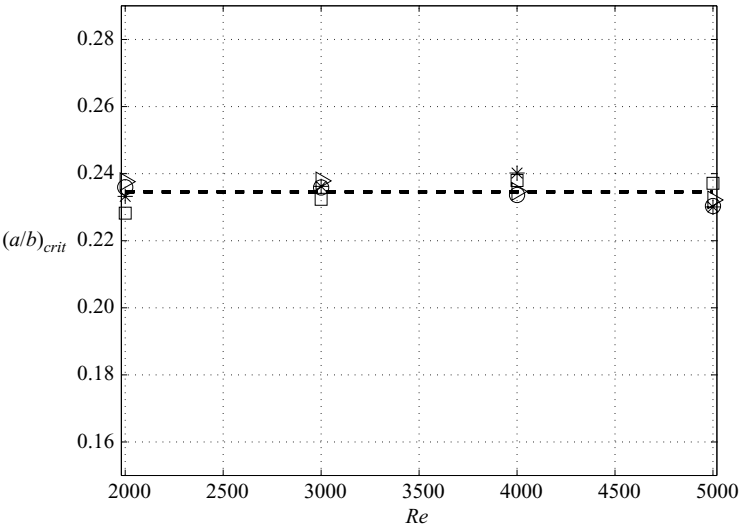

FIGURE 19. Critical aspect ratio, $(a/b)_{crit}$ according to equation (3.3), versus Re_Γ for different Fr. Dashed line represents the mean value, $(a/b)_{crit} \sim 0.235$. Symbols: ○, $Fr = \infty$; *, $Fr = 5$; ▷, $Fr = 3$; □, $Fr = 2$.

exchange band process, beyond which there is no reversal and merging will occur. The corresponding time, t^*_{CD}, is marked by the initiation of the contribution to $b^*(t)$ from the exchange band, Δb^*_{E} (figure 6*c*). This is also comparable to the time $a^2_\theta(t)$ deviates from linear growth. The critical state is therefore characterized by the aspect ratio (a/b) at $t^*_c = t^*_{\mathrm{CD}}$ for which the corresponding values of $a(t)$ and $b(t)$ are thereby determined. In the stratified flows, an effective a is determined from (3.3) at $t^*_c = t^*_{\mathrm{CD}}$. For all flows considered, $2000 \leqslant Re_\Gamma \leqslant 5000$ and $Fr = \infty$, 5, 3, 2, $(a/b)_{cr} = 0.235 \pm 0.006$ (figure 19). This is in agreement with the values $(a/b)_{cr} = 0.24 \pm 0.01$ reported by Meunier *et al.* (2002) for unstratified flow.

As discussed earlier, the latter portion of the convective/entrainment phase is clearly marked by the rapid, nearly linear decrease in $b^*(t)$ due to the exchange band contribution, Δb^*_{E} (e.g. figure 6*c*). We consider a time, t^*_{E}, as the effective start of core entrainment and defined by extending the linear portion of Δb^*_{E} to where it intersects with $\Delta b^*_{\mathrm{E}} = 0$. A plot of Δb^*_{E} versus $t^*_c - t^*_{\mathrm{E}}$ (figure 20) thereby overlays the exchange band process for the different Re_Γ and Fr flows. For all flows, the process proceeds at nearly the same rate. We therefore consider the core entrainment process, $t^*_{\mathrm{E}} < t^*_c < t^*_{\mathrm{CE}}$ (figure 17), to be independent of Re_Γ and Fr.

The merging time is therefore controlled by the processes prior to t^*_{E}, which depend on Re_Γ, Fr, and the initial aspect ratio. Thus, for the a_o/b_o considered, $t^*_{\mathrm{E}} = t^*_{\mathrm{E}}(Re_\Gamma, Fr)$. Figure 21 shows t^*_{E} versus Re_Γ for various Fr. In unstratified flow, a linear dependence is exhibited, consistent with results of Meunier *et al.* (2002), and is due to the predominance of diffusion prior to the exchange band process which is the dominant convective process. For the stratified flows, we see that there is a crossover Reynolds number ($Re_\Gamma \sim 2500$), above which convective merging is accelerated with respect to the unstratified flow at that Re_Γ, and below which merging is delayed. In stratified flow, convective effects (in the convective/deformation phase) become more significant due to the OSBV and SSBV. Since they arise due to the stirring of the density field by the co-rotating vortices, they have a timescale corresponding to the rotation, $t_c = 2\pi^2 {b_o}^2/\Gamma_o$, i.e. the turnover time. The effects of OSBV and SSBV will therefore

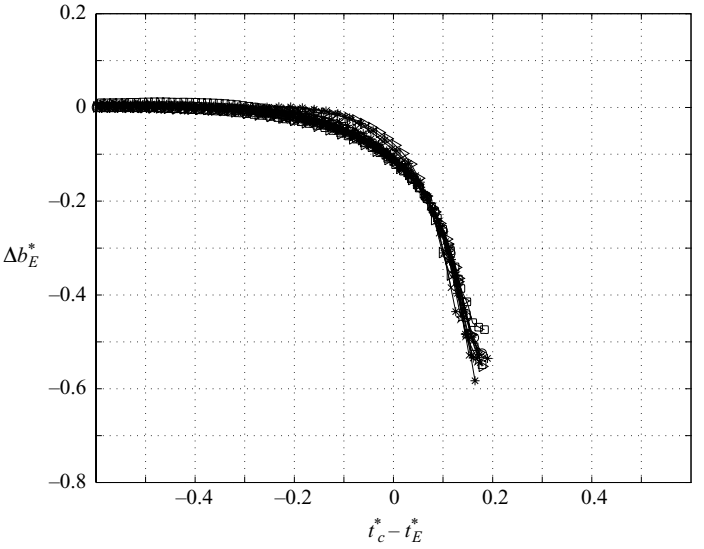

FIGURE 20. Exchange band contribution to separation distance development, $\Delta b_E^*(t)$, versus $t_c^* - t_{\mathrm{E}}^*$ for $Re_\Gamma = 2000, 3000, 4000, 5000$, $Fr = \infty, 5, 3, 2$.

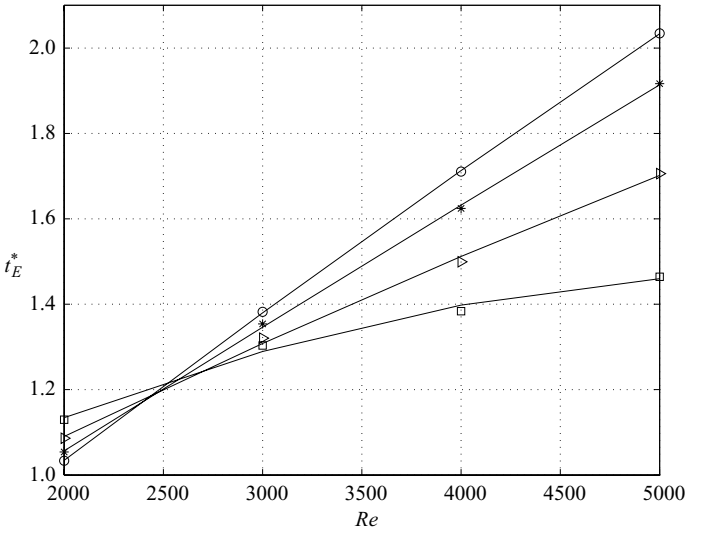

FIGURE 21. Effect of Re_Γ and stratification on merging time, t_{E}^*. Symbols: ○, $Fr = \infty$; ▷, $Fr = 3$; □, $Fr = 2$.

depend on the extent to which diffusion has developed the ω and $\boldsymbol{S}$ fields by the time OSBV/SSBV are generated. That is, for a given initial aspect ratio, the merging time in stratified flow will depend on the ratio of the diffusive time scale to the turnover time, and hence Re_Γ (3.8). From results of the unstratified flows, for $Re_\Gamma = 5000$, $t_{\mathrm{E}}^* = 2.02$, and for $Re_\Gamma = 2000$, $t_{\mathrm{E}}^* = 1.05$. Thus, the $Re_\Gamma = 5000$ flow rotates more than one revolution while the $Re_\Gamma = 2000$ flow just reaches one revolution prior to core entrainment. We may therefore expect their behaviors to differ with stratification. Results in figure 21 indicate that stratification accelerates merging for $Re_\Gamma = 5000$

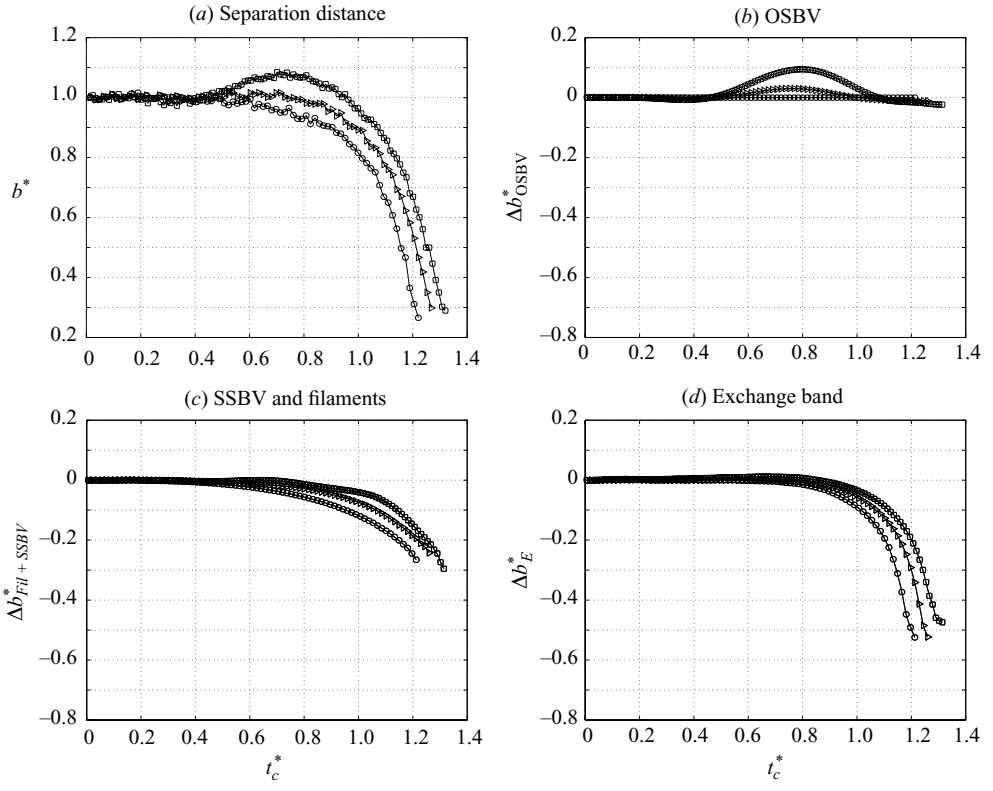

FIGURE 22. Contribution of flow regions to separation distance development, $\Delta b^*(t)$, for $Re_\Gamma = 2000$. Symbols: ○, $Fr = \infty$; ▷, $Fr = 3$; □, $Fr = 2$.

and delays merging for $Re_\Gamma = 2000$. In general, the Re_Γ dependency will be cyclic. The effects of OSBV and SSBV will also, of course, depend on their strength, and hence, Fr. Additionally, in the present study, we have considered only $a_o/b_o = 0.157$. In general, the crossover Reynolds number will vary with aspect ratio. As indicated by (3.8), the diffusion time will increase with smaller a_o/b_o. Additional simulation results (not shown) indicate a lower crossover Reynolds number for smaller a_o/b_o.

We now examine the $Re_\Gamma = 2000$ flow in which stratification delays merging. Figure 22(a) shows $b^*(t)$ for $Fr = \infty$, 3 and 2 and clearly indicates greater delay with increased stratification. Figure 22b–d shows the contribution of each flow region to $b^*(t)$. We observe that the OSBV (figure 22b) again acts to move the vortices apart during $0.5 \lesssim t_c^* \lesssim 0.8$, as in the $Re_\Gamma = 5000$ flow (figure 6). However, since this occurs near the end of the convective/deformation phase in this flow, the OSBV counteracts the initiation of convective/entrainment. Note that the amplitude of the OSBV contribution is reduced in comparison with that of $Re_\Gamma = 5000$ due to the increased diffusion of $\nabla\rho'$ (recall $Pr = 1$). In addition, since the core entrainment phase begins at approximately one full revolution, there is little SSBV generated (figure 22c) to assist in the merging process. Figure 23 indicates that $\langle P \rangle$ is generally reduced with increasing stratification. As the OSBV moves the vortices apart during $0.5 < t_c^* < 0.8$, the magnitude of the strain decreases as it does in the $Re_\Gamma = 5000$. This affects and controls the behavior of $\langle P \rangle$ (figure 23). Since $\langle P \rangle$ is reduced in the

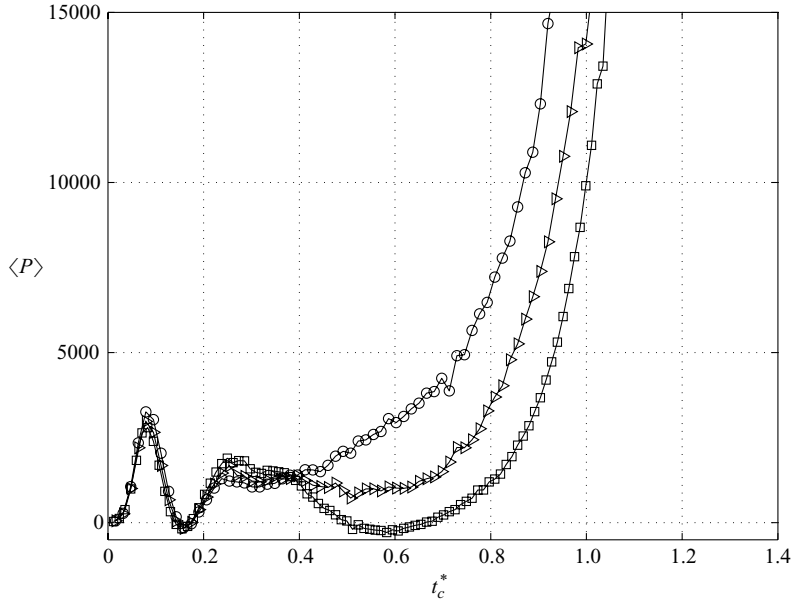

FIGURE 23. Time development of $\langle P\rangle = -\langle \nabla\omega^T \boldsymbol{S} \nabla\omega\rangle$, averaged over central region, for $Re_\Gamma = 2000$, $Fr = \infty$. Symbols: ○, $Fr = \infty$; ▷, $Fr = 3$; □, $Fr = 2$.

stratified flows, the tilting of ω contours is delayed. The core entrainment process therefore initiates later in time (figure 22*d*).

The final phase of the merging process is the diffusive/axisymmetrization phase ($t_c^* > t_{CE}^*$), during which $b(t)$ is reduced to zero and $a^2(t)$ eventually returns to linear growth for the single vortex. As stated earlier, this phase begins when b reaches approximately $0.20b_o - 0.25b_o$, at the end of the convective/entrainment phase at which point the inward velocities at the centroids are nearly zero. Although two ω maxima are still detected, inspection of the general flow structure shows that it is rotation-dominated and essentially consists of a single vortex. Thus, we consider this final phase, as a diffusion process in which the flow evolves towards axisymmetry. Details of this process which generally extends beyond the time at which $b^*(t)$ reaches zero, are beyond the scope of this work.

4. Summary

The merging of a pair of symmetric, horizontally oriented vortices in a viscous fluid with and without stable stratification has been investigated using two-dimensional numerical simulations. The flow conditions considered consist of a fixed initial aspect ratio $a_o/b_o = 0.157$, a range of circulation Reynolds numbers $2000 \leqslant Re_\Gamma \leqslant 5000$, and a range of stratification levels given by Froude numbers, $Fr = \infty, 5, 3, 2$. All of these flows are dominated by convection and diffusion, not by stratification ($Fr > 1$), and merging always occurs. The stratification essentially introduces a disturbance to the merging process. By determining its effects, we have obtained further insight and understanding of the fundamental physics of merging. We have also developed a generalized description of the merging process which consists of four phases: diffusive/deformation, convective/deformation, convective/entrainment, and diffusive/axisymmetrization. The phases are clearly defined and summarized in

§ 3.5. This new description of merger, which resolves the convective effects into two distinct processes, assists in accounting for the effects of stratification and allows for a more explicit determination of the critical aspect ratio.

Analysis of unstratified flow elucidates the key physical mechanisms of convective vortex merger. In particular, the deformation of the vortices is explained in terms of the interaction of vorticity gradient, $\nabla\omega$, and rate of strain, $\boldsymbol{S}$. During the diffusive/deformation phase, the vortices grow by diffusion. The induced strain of each of the vortices correspondingly spreads by diffusion and also develops through their mutual interaction. The interaction of $\nabla\omega$ and $\boldsymbol{S}$ is therefore established by diffusion. In the strain-dominated regions of the flow, and in particular in the vicinity of the center of rotation where the mutual interaction of strain is strongest, $\boldsymbol{S}$ becomes dynamically active and influences the vorticity field through amplification and reorientation of $\nabla\omega$, which produces a tilt in ω contours. The tilting and diffusion of ω leads to a misalignment of ω with respect to the streamlines. At the outer regions of the exchange band (near outer hyperbolic points), this causes ω to enter the outer-recirculation region and filamentation to occur. During the convective/deformation phase, the induced flow by the filaments acts to advect the vortices towards each other but does not drive the merger to completion. The reduction in separation distance enhances the strain at the central region. Here (near center hyperbolic point), the misalignment between ω and streamlines causes inner core ω to enter the exchange band and be advected away from its source core. This is the start of the convective/entrainment phase which is associated with a rapid decrease in the separation distance. The inner cores are thereby eroded, and at some point are themselves entrained. This is the predominant mechanism in convective merger. The circulation of the exchange band increases at the expense of that of the inner cores. The resulting fluid motion becomes rotation-dominated and transforms into what is essentially a single vortex at the end of the phase. The final diffusive/axisymmetrization phase is characterized by the slow diffusion of the two ω maxima and evolution towards axisymmetry.

With stably stratified ambient fluid, as the vortex pair rotates, it stirs the density field and generates both opposite-signed and same-signed vorticity through baroclinic torque. As in the unstratified flow, the interaction of $\nabla\omega$ and $\boldsymbol{S}$ is established by diffusion. The merging process in stratified flow therefore depends on the ratio of the diffusive time scale (growth of cores, establishment of $\nabla\omega$ and $\boldsymbol{S}$ interaction) to the turnover time (establishment of baroclinically generated vorticity, BV), i.e. the Reynolds number. A crossover Reynolds number ($Re_\Gamma \sim 2500$ for this initial aspect ratio) is found, above which convective merging is accelerated with respect to unstratified flow and below which merging is delayed. In general, the effect of the BV is similar to that of the filaments. The induced flow field will advect the vortices, either towards or away from each other, and this will modify the strain rate field, both in magnitude and direction. We distinguish this convective process by defining the convective/deformation phase, which may initiate while diffusion remains significant. Depending on the relative timescales, and stage of evolution (also initial aspect ratio), it may either enhance or hinder the $\nabla\omega$ amplification process. The strength of the BV depends on the level of stratification, as characterized by the Froude number. Therefore, initiation of the exchange band process and the convective/entrainment phase depends on both Re_Γ and Fr. Once initiated, the core entrainment process is relatively unaffected by either viscosity or level of stratification.

For both unstratified and stratified flows, we define the critical state of the flow to be the start of the convective/entrainment phase, beyond which there is no reversal and merging will occur. This is also approximately the time $a^2(t)$ deviates from linear

growth. However, since $b(t)$ may change significantly, the critical aspect ratio must be determined by $a(t)/b(t)$ at the time the exchange band process initiates. For all flows considered, $2000 \leqslant Re_\Gamma \leqslant 5000$ and $Fr = \infty, 5, 3, 2$, $(a/b)_{cr} = 0.235 \pm 0.006$, where the core size is effectively based on the second moment of vorticity. This is in agreement with values previously determined for unstratified viscous flows (Meunier *et al.* 2002).

The results presented in this study apply to pairs of symmetric (equal) co-rotating Gaussian vortices at moderate Re_Γ. Further studies should consider unequal vortices, other vorticity distributions, and higher Reynolds numbers. Vortex pairs in these flows may behave quite differently (Dritschel & Waugh 1992). The present study provides fundamental insight into vortex interaction and the merging process. It also provides a framework with which these flows may be analyzed.

The authors would like to acknowledge Dr Patrice Meunier for helpful discussions. The first author received support from the ARCS (Achievement Rewards for College Scientists) foundation.

REFERENCES

Brandt, L. K. & Nomura, K. K. 2006 The physics of vortex merger: further insight. *Phys. Fluids* **18**, 1–4.

Brandt, S. A. & Iversen, J. D. 1977 Merging of aircraft trailing vortices. *J. Aircraft* **14**, 1212.

Cerretelli, C. & Williamson, C. H. K. 2003 The physical mechanism for vortex merging. *J. Fluid Mech.* **475**, 41–77.

Dritschel, D. G. 1985 The stability and energetics of corotating uniform vortices. *J. Fluid Mech.* **157**, 95–134.

Dritschel, D. G. 1998 On the persistence of non-axisymmetric vortices in inviscid two-dimensional flows. *J. Fluid Mech.* **371**, 141–155.

Dritschel, D. G. 2002 Vortex merger in rotating stratified flows. *J. Fluid Mech.* **455**, 83–101.

Dritschel, D. G. & Waugh, D. W. 1992 Quantification of the inelastic interaction of unequal vortices in two-dimensional vortex dynamics. *Phys. Fluids* A **4**, 1737–1744.

Gerz, T., Schumann, U. & Elghobashi, S. 1989 Direct simulation of stably stratified homogeneous turbulent shear flows. *J. Fluid Mech.* **200**, 563–594.

Griffiths, R. W. & Hopfinger, E. J. 1987 Coalescing of geostrophic vortices. *J. Fluid Mech.* **178**, 73–97.

von Hardenberg, J., McWilliams, J. C., Provenzale, A., Shchepetkin, A. & Weiss, J. B. 2000 Vortex merging in quasi-geostrophic flows. *J. Fluid Mech.* **412**, 331–353.

Huang, M. J. 2005 The physical mechanism of symmetric vortex merger: A new viewpoint. *Phys. Fluids* **17**, 1–7.

Jeong, J. & Hussain, F. 1995 On the identification of a vortex. *J. Fluid Mech.* **285**, 69–94.

Kimura, Y. & Herring, J. R. 2001 Gradient enhancement and filament ejection for a non-uniform elliptic vortex in two-dimensional turbulence. *J. Fluid Mech.* **439**, 43–56.

Koop, C. G. & Browand, F. K. 1979 Instability and turbulence in stratified fluid with shear. *J. Fluid Mech.* **93**, 135–159.

Le Dizes, S. & Verga, A. 2002 Viscous interactions of two co-rotating vortices before merging. *J. Fluid Mech.* **467**, 389–410.

Melander, M. V., McWilliams, J. C. & Zabusky, N. J. 1987 Axisymmetrization and vorticity-gradient intensification of an isolated two-dimensional vortex through filamentation. *J. Fluid Mech.* **178**, 137–159.

Melander, M. V., Zabusky, N. J. & McWilliams, J. C. 1988 Symmetric vortex merger in two dimensions: Causes and conditions. *J. Fluid Mech.* **195**, 305–340.

Meunier, P. 2001 Etude experimentale de deux tourbillons co-rotatifs. PhD dissertation, Université d'Aix-Marseille I, France.

Meunier, P., Ehrenstein, U., Leweke, T. & Rossi, M. 2002 A merging criterion for two-dimensional co-rotating vortices. *Phys. Fluids* **14**, 2757–2766.

Meunier, P., Le Dizes, S. & Leweke, T. 2005 Physics of vortex merging. *CR Physique* **6**, 431–450.

Meunier, P. & Leweke, T. 2001 Three-dimensional instability during vortex merging. *Phys. Fluids* **13**, 2747–2750.

Nomura, K. K. & Post, G. K. 1998 The structure and dynamics of vorticity and rate of strain in incompressible homogeneous turbulence. *J. Fluid Mech.* **377**, 65–97.

Nomura, K. K., Tsutsui, H., Mahoney, D. & Rottman, J. W. 2006 Short-wavelength instability and decay of a vortex pair in a stratified fluid. *J. Fluid Mech.* **553**, 283–322.

Overman, E. A. & Zabusky, N. J. 1982 Evolution and merger of isolated vortex structures. *Phys. Fluids* **25**, 1297–1305.

Patnaik, P. C., Sherman, F. S. & Corcos, G. M. 1976 A numerical simulation of Kelvin–Helmholtz waves of finite amplitude. *J. Fluid Mech.* **73**, 215–240.

Pawlak, G. & Armi, L. 1998 Vortex dynamics in a spatially accelerating shear layer. *J. Fluid Mech.* **376**, 1–35.

Pawlak, G. & Armi, L. 2000 Mixing and entrainment in developing stratified currents. *J. Fluid Mech.* **424**, 45–73.

Protas, B., Babiano, A. & Kevlahan, N. K.-R. 1999 On geometrical alignment properties of two-dimensional forced turbulence. *Physica* D **128**, 169–179.

Rossow, V. J. 1977 Convective merging of vortex cores in lift-generated wakes. *J. Aircraft* **14**, 283–290.

Saffman, P. G. 1992 *Vortex Dynamics*. Cambridge University Press.

Saffman, P. G. & Szeto, R. 1980 Equilibrium shapes of a pair of equal uniform vortices. *Phys. Fluids* **23**, 2339–2342.

Schowalter, D. G., Van Atta, C. W. & Lasheras, J. C. 1994 A study of streamwise vortex structure in a stratified shear layer. *J. Fluid Mech.* **281**, 247–291.

Velasco Fuentes, O. U. 2005 Vortex filamentation: its onset and its role on axisymmetrization and merger. *Dyn. Atmos. Oceans* **40**, 23–42.